LIÈGE université Library

https://lib.uliege.be

https://matheo.uliege.be

Final work : Numerical analysis of surface roughness impact on the aerodynamic damping of an axial transonic compressor

Auteur : Canela Curiel, Pablo
Promoteur(s) : Salles, Loïc
Faculté : Faculté des Sciences appliquées
Diplôme : Master en ingénieur civil en aérospatiale, à finalité spécialisée en "turbomachinery aeromechanics (THRUST)"
Année académique : 2022-2023
URI/URL : http://hdl.handle.net/2268.2/18380

Avertissement à l'attention des usagers :

Tous les documents placés en accès ouvert sur le site le site MatheO sont protégés par le droit d'auteur. Conformément aux principes énoncés par la "Budapest Open Access Initiative"(BOAI, 2002), l'utilisateur du site peut lire, télécharger, copier, transmettre, imprimer, chercher ou faire un lien vers le texte intégral de ces documents, les disséquer pour les indexer, s'en servir de données pour un logiciel, ou s'en servir à toute autre fin légale (ou prévue par la réglementation relative au droit d'auteur). Toute utilisation du document à des fins commerciales est strictement interdite.

Par ailleurs, l'utilisateur s'engage à respecter les droits moraux de l'auteur, principalement le droit à l'intégrité de l'oeuvre et le droit de paternité et ce dans toute utilisation que l'utilisateur entreprend. Ainsi, à titre d'exemple, lorsqu'il reproduira un document par extrait ou dans son intégralité, l'utilisateur citera de manière complète les sources telles que mentionnées ci-dessus. Toute utilisation non explicitement autorisée ci-avant (telle que par exemple, la modification du document ou son résumé) nécessite l'autorisation préalable et expresse des auteurs ou de leurs ayants droit.

MSc in Turbomachinery Aeromechanics (THRUST)

Université de Liège, School of Engineering and Computer Science

Academic year 2022-2023

Master Thesis

Numerical analysis of surface roughness impact on the aerodynamic damping of an axial transonic compressor

Author:

Pablo Canela Curiel

Supervisors (KTH): Carlos Tavera Guerrero & Nenad Glodic

Promoter (ULiège): Loïc Salles

Graduation Studies conducted for obtaining the Master's degree in Civil engineer in aerospace, specialized in "turbomachinery aeromechanics"

Liège, August 2023

Members of the jury:

Koen Hillewaert
Universitè de Liège, Faculty of Engineering (Liège, Belgium)
Department of Aerospace and Mechanical Engineering

Grigorios Dimitriadis
Universitè de Liège, Faculty of Engineering (Liège, Belgium)
Department of Aerospace and Mechanical Engineering

Loïc Salles, *ULiège academic promoter*
Universitè de Liège, Faculty of Engineering (Liège, Belgium)
Department of Aerospace and Mechanical Engineering

Carlos Tavera Guerrero, *KTH supervisor*
KTH Royal Institute of Technology (Stockholm, Sweden)
Department of Heat and Power Technology

ABSTRACT

Current trends in advanced design of turbomachinery structures are leading to more loaded, lighter and slender blades. These characteristics make them prone to aeroelastic instabilities, such as flutter. Moreover, blades are continuously exposed to the incoming flow carrying pollutants and external particles that can affect the smoothness of the blade surface. It is well known the detrimental effect that surface roughness has in the performance of the machine. However, there is a lack of studies regarding the effects of surface roughness in the aeroelastic stability. This is the main focus of this thesis.

Studies regarding surface roughness modelling are scattered and contain very diverse information and conclusions on the topic. There exists a wide range of parameters and equations to correlate physical measurements and equivalent sandgrain roughness height, k_s. From a turbomachinery perspective, a literature review on the current stage of surface roughness modelling has been performed. A final correlation is chosen as the most suitable to model surface roughness in compressors, based on the simplicity to measure the physical parameters included, and the high degree of correlation with k_s.

A numerical study using ANSYS CFX is performed to evaluate the impact of surface roughness in the aeroelastic stability of a transonic axial compressor. The study case is the first stage (R1S1B) of the VINK compressor. First, a set of 7 different k_s values are evaluated with a steady-state analysis. Results show a negative impact on performance, reducing efficiency, mass flow rate and pressure ratio. Due to blockage effects, a change in incidence angle is found, causing a change in passage shock location and strength. A smaller set of just 3 k_s values is selected for the flutter analysis just on the rotor domain. The aerodynamic damping is computed for nodal diameters 0, ±3 and ±15. Results show different trends depending on the nodal diameter evaluated. According to the study, surface roughness has a small positive impact for the least stable modes, slightly increasing the aerodynamic damping. The contrary happens for the most stable NDs, where surface roughness induces a reduction in the aerodynamic damping, but without being enough to shift the value to the unstable region. Some limitations are encountered, mainly due to the oversimplification of roughness with k_s, and the assumption of a tuned system, removing the effects of mistuning. Future work is proposed in order to reduce and overcome the limitations here identified.

Keywords: Surface roughness correlation, equivalent sandgrain height, transonic compressor, flutter, aerodynamic damping, VINK, CFD

ACKNOWLEDGEMENTS

First of all, I would like to express my complete gratitude to my tutor, Carlos Tavera. Thank you for giving me the opportunity to work with you, for all the time you have dedicated to me, and for never stopping believing in me. Also, I wanted to thank Prof. Loïc Salles, for guiding me and giving me support during these last 6 months.

I also want to thank all the people of the THRUST programme. To Nenad Glodic for opening me the door to this wonderful experience. Also to all my friends who have been part of these two years of my life between Stockholm, Liège, and Madrid.

A big thank you to my family for supporting me at all times. To my parents and brother for always taking care of me and for the warm welcomes every time I came back home. Finally, to Julia for being the most important part in these two years of my life (and for making me the list of acronyms).

CONTENTS

LIST OF FIGURES

LIST OF TABLES

LIST OF ACRONYMS

BTW Backward Travelling Wave

DNS Direct Numerical Simulation

FTW Forward Travelling Wave

GCL Geometric Conservation Law

IBPA Interblade Phase Angle

IGV Inlet Guide Vanes

LEO Low Engine Order

LES Large Eddy Simulation

LHS Left Hand Side

NC Near Choke

NCl Nodal Circle

ND Nodal Diameter

NS Near Stall

NSV Non-Synchronous Vibration

OGV Outlet Guide Vanes

OP Operating Point

PE Peak Efficiency

PS Pressure Surface

RANS Reynolds Average Navier-Stokes

RHS Right Hand Side

SS Suction Surface

SST Shear Stress Transport

TKE Turbulent Kinetic Energy

TWM Travelling Wave Mode

URANS Unsteady Reynolds Average Navier-Stokes

VINK Virtual Integrated Compressor Demonstrator

WWD Wall Work Density

ZZENF Zigzag Excitation Line in Nodal Diameter vs. Frequency

1B First Bending Mode

1T First Torsion Mode

2B Second Bending Mode

LIST OF SYMBOLS

A_f	Frontal area of just one roughness element	[L^2]
A_m	Fourier coefficients	
$A_{\max}$	Maximum oscillation amplitude	[L]
A_s	Windward wetted area of one single roughness element	[L^2]
B	Log-layer constant (equal to 5.2)	-
C_{Aero}	Aerodynamic damping matrix	
C_{Struct}	Structural damping matrix	
c	Blade true chord	[L]
ES	Effective Slope	-
K_{Aero}	Aerodynamic stiffness matrix	
K_{Struct}	Structural stiffness matrix	
KE_{ave}	Average Kinetic Energy	[M L^2/T^2]
k_{red}	Reduced Frequency	-
k_s	Sandgrain roughness height	[L]
k_u	Roughness kurtosis	-
k^+	Roughness Reynolds number	-
L_x	Streamwise sample length	[L]
L_y	Spanwise sample length	[L]
M_{isen}	Isentropic Mach number	-
M_{Struct}	Structural mass matrix	
$\dot{m}_{corr}$	Corrected mass flow rate	[M/T]
Ra	Arithmetic average roughness height	[L]
Rq	Root mean square roughness height	[L]
Rz	peak-to-valley roughness height	[L]
S	Reference surface area before the addition of roughness	[L^2]
S_f	Total frontal area of the roughness	[L^2]
s_k	Roughness skewness	-
t_r	Residence time	[T]
U^+	Near-wall velocity function	-
$U_{\infty,rotor}$	Relative flow velocity at the inlet of the rotor domain	[L/T]
u_τ	Friction velocity	[L/T]
u^*	Alternate velocity scale	[L/T]

W_{cycle}	Work-per-cycle	[M L^2/T^2]
W_j	Velocity of the control volume boundary	[L/T]
y	Wall Location	[L]
y^+	Dimensionless distance from the wall	-
y^*	Dimensionless scaled distance from the wall	-
Y_R	Rotor total pressure loss coefficient	-
α_j	Local streamwise forward-facing surface angle	-
α_{rms}	Root-mean-square local slope angle	-
Δ	Roughness element size distribution parameter	-
ΔU^+	Roughness function	-
Δy	Distance from the wall	[L]
δ	Logarithmic decrement	-
ζ	Critical Aerodynamic Damping	-
η_p	Polytropic Efficiency	-
κ	Von-Karman Constant (equal to 0.41)	-
Λ_s	Shape-Density Parameter	-
λ	Solidity parameter	-
ν	Kinematic viscosity	[L^2/T]
$\Pi_{t,13}$	Stage Total Pressure Ratio	-
ω	Oscillation frequency	[1/T]

1. INTRODUCTION

1.1. Motivation

Performance and efficiency are the two main objectives that are sought to be achieved when designing any kind of machine. This outcome acquires even more importance in the field of gas turbines and turbomachinery. Efficiency and performance degradation or improvement results in a huge impact regarding both economical and environmental aspects. With most of the main concepts already designed and implemented, industry is currently mainly focused on optimising more specific aspects and performing a more in-depth research on the design of the machines [1]. Among all the current research trends, deterioration of materials and components during service appears to be one of the most active [2]. Axial compressors and turbines are exposed to a large number of degradation mechanisms caused by foreign matter ingestion, combustion products or high temperature among others. Compressor and turbine blades are the main components that suffer the consequences of these degradation processes leading to changes on their original geometry. For instance, reduction of the leading edge, clogging of cooling orifices in the case of turbines, or changes in the smoothness of their surface [3]. The latter is the main focus of this thesis.

Surface roughness is defined by Trevisani et al. [4] as "local variations in elevation which indicate less and less local smoothness" or in a simpler way as the lack of smoothness of a surface. This can be inherent to a surface or material, or it can be caused by the interaction of the material with a second body. Regarding turbomachinery blades, these are designed to be as smooth as possible to favor aerodynamic features, thus maximizing system efficiency [5]. However, compressor and turbines in gas turbines do not operate in a pure environment. These are directly affected by external matter that interact with the surface material provoking a complete or partial loss of the original smoothness of the blades. This is inevitable, and the consequences vary in a range of only a small efficiency drop to a complete burst of the engine in the worst case [6, 7]. Due to this, there is a need to model and test the effects of surface roughness from the point of view of aeromechanics as accurate as possible in order to predict its evolution and be able to mitigate its consequences with respect with the original machine design [8].

During the last decades, a lot of effort has been put into modeling surface roughness in a

controlled way in order to be able to study its effects on the flow near the wall [2, 5, 6, 8, 9]. Among all this work, it has been found that modeling 3D random surface roughness to represent what can be seen in real systems is very challenging. Normally only the overall effects can be evaluated without being able to study the specific features of the roughness distribution, such as the density of peaks and valleys, local slope, shape, etc. [9, 10]. Therefore, the importance of an accurate numerical modeling arises. This will allow to draw the surface roughness implementing the desired properties separating the influence of the distinct roughness features. However, there are currently big limitations regarding the implementation of roughness in CFD codes, mainly due to the high computational cost required to discretize the geometry up to a microscopic scale inside domains of larger orders of magnitude of size [3, 9, 11].

An accurate numerical modeling in the field of fluid dynamics is always very demanding, even more when facing complex geometries that require very fine meshes to catch every feature of the flow. This applies in the case of surface roughness modeling. To represent exactly the local flow field under the influence of non smooth surfaces, the 3D random distribution of surface roughness should be modelled with a fine mesh at a microscopic scale [3, 12]. This can be done for one particular case, but a family of solutions may be required and the time window in order to simulate them is not affordable in most cases. Therefore, there is a need for proper simplifications in codes at the cost of accuracy. The current implementation features the input of an equivalent sand grain height (k_s) which represents a surface roughness with the same effect on skin friction as a uniform layer of actual sandgrains of equal diameter [8, 9, 11]. This roughness scale was introduced and developed by Nikuradse [13] and Slichting [14] in different works. This scale is recognised as the universal parameter that relates the effects of roughness and skin friction. However, the original equivalence proposed by Schlichting is not appropriate for predicting heat transfer or boundary layer transition as it was fitted only for skin friction. Despite of this, Nikuradse and Schlichting works set the start of a large number of studies trying to find proper correlations between the actual shape of the roughness and the equivalent sandgrain without converging to an unique formulation [3, 15]. Different roughness features, curve fitting and experimental validation have been used sparsely ending up with a extensive list of very diverse correlations. For this reason, there exists a motivation of finding an universal representation that would use the maximum amount of information to describe the features of roughness. However, this still represents an enormous lack of information regarding the local distribution of roughness [10, 16]. How does the flow behaves when encountering of a sudden peak or valley? Does it matter if the roughness is peak or valley dominated?

The following sections are intended to describe the current state of surface roughness characterisation and to find a correlation to describe surface roughness in general, but more specifically in the field of axial turbomachinery, based on its topology represented by its local features and its statistical moments. Numerous studies have investigated the effects of surface roughness

on turbomachinery performance variables, such as efficiency, total pressure ratio, or mass flow rate [2, 3, 5, 17, 18]. However, there is a lack of studies in this field regarding the interaction between surface roughness and the aeroelastic behaviour of turbomachinery components. This thesis work will focus on the effect of surface roughness from an aeroelastic perspective to study its consequences on aerodynamic damping and stability.

1.2. Objectives

This section presents the objectives of this Thesis displayed following a chronological order.

- Selection of a physical-to-equivalent sandgrain roughness correlation that accurately represents the major properties of surface roughness, keeping in mind its feasibility in terms of measurement processes and numerical implementation on CFD software.
- Definition and simulation of a set of steady-state cases for a set of rough surfaces. This includes studies on the selection of the turbulence model, mesh and operational point.
- Definition and simulation of set of unsteady-state simulations performing a flutter analysis for the same set of rough surfaces defined during the steady-state cases.
- Identification of the effect of surface roughness on the wall work density and aerodynamic damping.

These objectives are discussed in detail in the next sections, and are intended to provide the reader with a clear overall view of the project.

2. STATE OF THE ART

This chapter presents the state of the art and theoretical concepts regarding the two main topics of this thesis, surface roughness and aeroelasticity. The first section covers all the concepts about surface roughness modeling, starting from the early stages of roughness investigations and ending with a chosen physical-to-sandgrain roughness correlation suitable for turbomachinery applications. The second section deals with all the theory behind aeroelasticity in turbomachinery, with a specific focus in flutter.

2.1. Surface roughness modeling

The first studies on the effect of surface roughness in flow were carried out by Nikuradse in 1930 [13]. Nikuradse roughness experiments in pipes focused on finding relationships between wall roughness and Reynolds number ranging from 600 to 10^6, velocity profiles or mixing length. Nikuradse introduced the nondimensional roughness parameter for the first time, also known as the roughness Reynolds number as it is defined in a similar way, using the sandgrain height, k_s, the friction velocity, u_τ and the kinematic viscosity, ν:

$$k^+ = \frac{k_s u_\tau}{\nu} \tag{2.1}$$

With this scale, Nikuradse was able to define three roughness regimes: hydraulically smooth, transitionally rough, and fully rough. These three regimes determine the features of turbulent flows with respect to the roughness level as follows:

- Hydraulically smooth wall ($0 \leq k^+ < 5$): The roughness elements are completely placed inside the viscous sublayer and therefore the effect produced on the skin friction and drag coefficients is negligible or even null.
- Transitionally rough ($5 \leq k^+ \leq 70$): Some of the roughness elements are thicker than the viscous sublayer and start to disturb it. Both viscous and pressure forces influence the skin friction and drag coefficients.
- Fully rough ($k^+ > 70$): The viscous sublayer is completely destroyed and the logarithmic profile is shifted downward. Viscous effects are negligible compared to the pressure effects.

The roughness in Nikuradse's experiments was modeled by sand grains with a diameter of k_s. A main outcome of Nikuradse's work was his conclusion on the modification of the turbulent boundary layer "law of the wall" due to the presence of roughness. He found out that an increase on surface roughness, caused a downward shift on the law of the wall as a function of k^+:

$$U^+ = \frac{1}{\kappa} \ln y^+ + B - \Delta U^+ \tag{2.2}$$

where ΔU^+ is known as the roughness function, directly related to k^+, hence also to k_s. In this way and thanks to the work by Schlichting [14] defining the equivalent sandgrain height, k_s, this can be used as the key parameter to calculate the skin friction parameter due to roughness effects. However, this variable is not a physical one, and thus it cannot be extracted directly from measurements on rough surfaces. Physical-to-sandgrain roughness height and the exact onsets for the roughness regimes have been topics extensively discussed through the literature. Bons in 2010 [3] published a work gathering a large set of 23 very different correlations, dating from 1962 to 2006, connecting k_s with diverse measurable roughness variables. From this work, it is impossible to extract a common trend or a preferred correlation. Every author found their own correlation that best fitted their data, here the motivation why Bons [3] performed this extensive review. The most common parameter among all these equations is the arithmetic average roughness height, *Ra*, but also correlations including the RMS (Root Mean Square) roughness height, *Rq* or R_{rms}, the peak-to-valley roughness, *Rz*, roughness shape parameter, Δ_s, etc. All these parameters are explained in detail later in this section. There is also a big issue concerning this correlations and it is the fact that not even the ones using the same roughness parameter, share the same coefficients. It can be concluded from Bons work that the correlations using *Ra* have the shape $k_s = C\,Ra$, and that C can vary in a range of 1 to 16.

Goodhand *et al.* [16] account for the limitations of just using one physical roughness parameter to describe surface roughness. It was concluded that the topography of the roughness cannot be ignored. Using just *Ra* to model surface roughness represents a lack of information leading to poor or wrong characterization of the flow. This conclusion was also achieved by Bogard *et al.* [19] in a work directly applied to real turbine roughness. Goodhand [16] also performed a study to determine which parameter will better represent roughness topography. The chosen parameters were the skewness, defined as the peak-valley density, and the roughness slope, known as the average slope that the flow sees. The tests were carried out in a transonic wind tunnel for Reynolds number varying from 10^5 to 2×10^6. The blades were made of different materials surface treated by shot blasting and polishing to obtain a diverse range of roughness topographies, where only the suction surface was considered, known to be the surface most affected by changes in roughness. The main conclusion of the work states that roughness topography is essential to describe roughness, however there is no agreement on which parameter better describes it. Roughness slope seems to predict better the thickening of the boundary layer, but it fails at assessing the onset of transition.

Kadivar *et al.* (2021) [15] performed a study of the current state of surface roughness modeling, describing a more updated review of surface roughness correlations, but also going through the main theories and hypotheses in this field in order to give a whole picture of it to the reader. Kadivar gives a very detailed description of the most common surface roughness parameters before showing the main correlations. Among these parameters, the most interesting ones for the characterisation of surface roughness are the statistical based parameters, such as the arithmetical roughness height, Ra, root-mean-square height, Rq, skewness, s_k, and kurtosis, k_u, the Effective Slope, ES, the solidity, λ, and shape parameters, A_f/A_s, the shape-density parameter, Λ_s, and the root-mean-square surface slope angle, α_{rms}, as demonstrated by other works by Flack and Schultz [10, 20, 21], Gilge *et al.* [7], Bons [17, 22] and Sigal and Danberg [23]. The definition and mathematical characterisation of these parameters are detailed in the following list:

- **Arithmetic average roughness height** (Ra): Average roughness of the profile about a mean line [24]. It is known to be the most common parameter used for a simplified representation of surface roughness. In 2D is given by Equation 2.3 [16]:

$$Ra = \frac{1}{L}\int_0^L |z(x) - \mu| dx, \tag{2.3}$$

  for a measured length, L, roughness height, $z(x)$ and mean-line displacement, μ.

- **Peak-to-valley roughness height** (Rz): Mean maximum peak-to-valley height of a certain subset of the surface averaged by the total number of measured areas. For a given subset, in the case of the ten-point height value it is computed as [24]:

$$Rz_i = \frac{\sum_{j=1}^{5} |z_{pj}| - \sum_{j=1}^{5} |z_{vj}|}{5}, \tag{2.4}$$

  where z_{pj} and z_{vj} are the five highest peaks and deepest valleys, respectively. This parameter is more sensitive to sudden high peaks or deep valleys than Ra or Rq [15], hence it is widely used to scale roughness height in numerous industrial studies.

- **Root-mean-square roughness height** (Rq): Square root of the second moment of statistics. It is known to give a better estimation of the roughness height. In 2D, Rq is expressed as [16]:

$$Rq = \sqrt{\frac{1}{L}\int_0^L (z(x) - \mu)^2 dx} \tag{2.5}$$

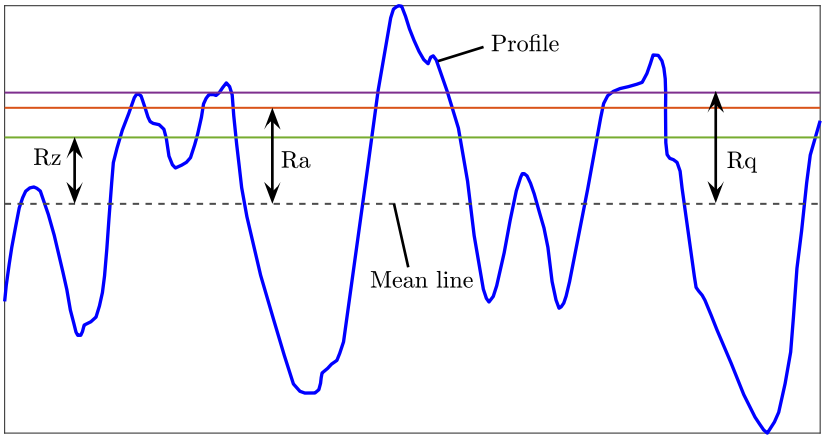

Fig. 2.1. Schematic representation of roughness height parameters: *Ra, Rq, Rz*

- **Roughness skewness** (s_k): Skewness represents the third moment of statistics and provides a measure of the profile symmetry, physically determining if the profile is valley or peak dominated as the skewness is negative or positive, respectively [10]. Gaussian distribution adopts a value of zero, meaning an equal number of peaks and valleys. For a given 2D sample, skewness is computed as [24]:

$$s_k = \frac{1}{Rq^3} \int_{-\infty}^{+\infty} (z(x) - \mu)^3 p(z) dx, \tag{2.6}$$

with $p(z)$ being the normal Gaussian distribution. Refer to [24] for more details on $p(z)$.

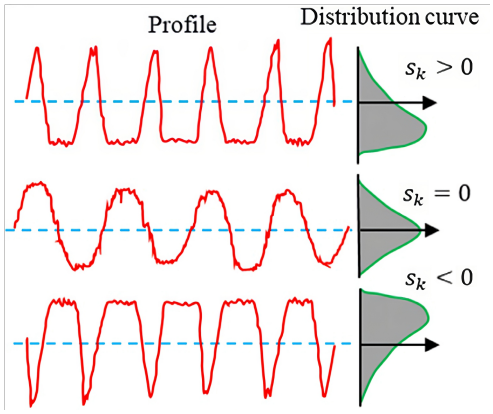

Fig. 2.2. Schematic representation of skewness [15]

- **Roughness kurtosis** (k_u): Kurtosis is the fourth moment of statistics and gives a measure of the sharpness of the profile. For a normal distribution k_u collapses to a value of 3, meaning that a $k_u > 3$ presents a distribution with relatively many peaks and low valleys and the opposite when $k_u < 3$ [15]. In a similar way as s_k, kurtosis is defined by [24]:

$$k_u = \frac{1}{Rq^4} \int_{-\infty}^{+\infty} (z(x) - \mu)^4 p(z) dx \tag{2.7}$$

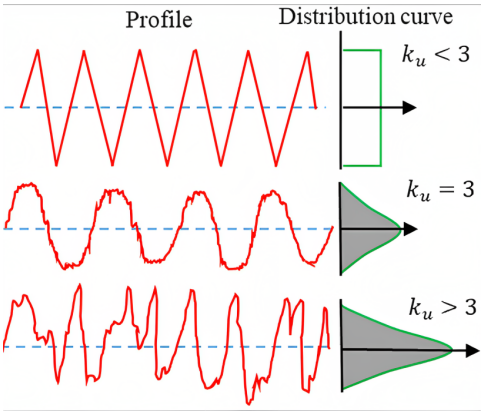

Fig. 2.3. Schematic representation of kurtosis
[15]

- **Effective Slope** (ES): The Effective Slope is defined as the average value of the magnitude of the slope of the roughness element [15]. This scale is used to distinguish between wavy surfaces (ES<0.35) from actual surface roughness (ES>0.35) [25, 26]. This is a very important threshold as wavy surfaces appear to be highly influenced by slope related parameters and not by roughness height related parameters. ES in a 3D roughness distribution is computed as [26]:

$$ES = \frac{1}{L_x L_z} \int_0^{L_x} \int_0^{L_z} \left| \frac{\partial k(x,z)}{\partial x} \right| dxdz, \tag{2.8}$$

where L_x and L_z are the streamwise and spanwise sample lengths, and k is the roughness amplitude.

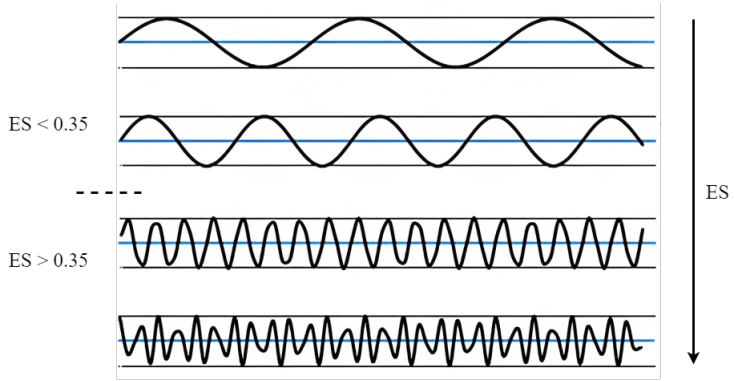

Fig. 2.4. Schematic representation of profiles with varying Effective Slope.
Image adapted from [15].

- **Solidity parameter** (λ): Solidity is defined as the ratio of total projected frontal roughness area, S_f to total area without roughness elements, S (S_f/S). It has been shown that solidity can be expressed as half the value of the effective slope, thus: $ES = 2\lambda$.

- **Shape-Density Parameter** (Λ_s): Shape-Density parameter, firstly introduced by Sigal and Danberg [23], gives information about the concentration of asperities for a given

sample measured and it combines the effect of solidity with the frontal area of just one roughness element (A_f) and the windward wetted area of one single roughness element (A_s) as follows:

$$\Lambda_s = \left(\frac{S}{S_f}\right)\left(\frac{A_f}{A_s}\right)^{-1.6} \tag{2.9}$$

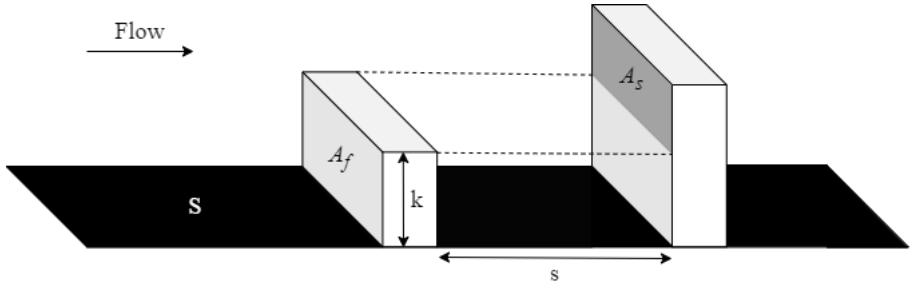

Fig. 2.5. Schematic representation of shape-density parameter: A_f, A_s and S (with s being the spacing between two given roughness elements, and k being the height of a single roughness element). Image adapted from [27]

As this parameter clearly implements the solidity function, it can be shown that: $\Lambda_s \propto (2\lambda)^{-1} = ES$.

- **Root-mean-square local slope angle** (α_{rms}): The local slope angle, introduced by Bons [17], is defined as the local streamwise forward-facing surface angle computed for each streamwise trace. It can be computed as follows in a discrete way [28]:

$$\alpha_j = \tan^{-1}\left(\frac{h_{j+1} - h_j}{\Delta s}\right), \tag{2.10}$$

where α_j is each value for the local streamwise forward-facing surface angle, Δs is the spacing between two consecutive asperities, and h_j is the height corresponding to each element. Then to compute α_{rms}, the root-mean-square formula is applied.

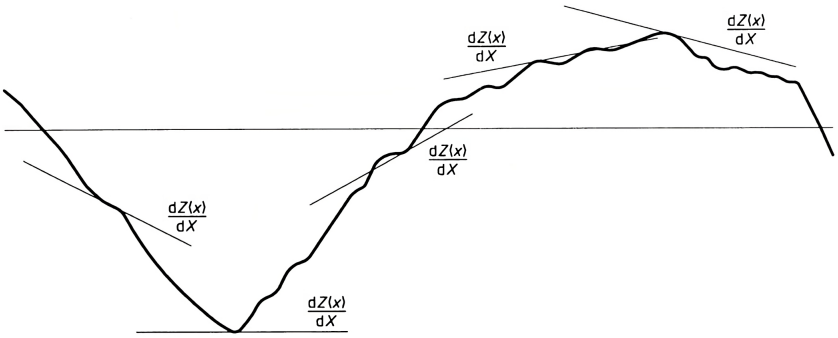

Fig. 2.6. Schematic 2D representation of local slope angle, expressed in this case as $\frac{dZ(x)}{dx}$ [29].

Kadivar [15] presents a list with a set of correlations implementing most of the parameters above detailed. This updated set of correlations implement more than just one roughness parameter combining parameters such as Rq and s_k (Flack *et al.* [10, 30]) or using derived variables such as Λ_s [17, 23] or α_{rms} [17, 31, 32].

Flack *et al.* (2010-2020) [10, 20, 21, 30, 33, 34] present a series of papers aiming to find the most representative roughness parameter for the characterisation of surface roughness in both the fully rough and transitionally rough regimes. In [10], Flack *et al.* use a procedure to compute the roughness function experimentally, measuring the friction coefficient, allowing a comparison to Nikuradse's roughness function as shown in the following set of relationships:

$$\Delta U^+ = f(C_{f,r}) - f(C_{f,s}) \tag{2.11}$$

$$\Delta U^+ = \frac{1}{\kappa} \ln k_s^+ + B - 8.5 \tag{2.12}$$

where $B \approx 5.0$ is the smooth-wall additive constant, and $\kappa = 0.41$ is the Von-Karman constant. Equation 2.12 is known as the fully rough asymptote for a sandgrain roughness type. In this paper, the development of a new roughness correlation was presented for the fully rough regime. Statistic surface moments were used in order to overcome the difficulties encountered when evaluating direct geometrical surface roughness parameters such as spacing, shape or slope parameters. It was concluded that Rq and s_k have the highest degree of correlation with k_s. The proposed correlation is shown in Equation 2.13:

$$k_s = 4.43Rq(1 + s_k)^{1.37} \tag{2.13}$$

This correlation shows very good agreement for k_s and C_f predictions when compared to geometrical parameters such as Λ_s. This correlation was performed just for positive skewed surfaces. Aditionally, Flack *et al.* [30] performed a study with several self-built surfaces with the desired properties generated by a high precision 3D printer. The positive, zero and negative skewness effects were identified leading to three different correlations with the same form as in Equation 2.13. It was also concluded that most surfaces converge to a Nikuradse-type roughness function. However, there is still a gap to cover in the case of highly skewed surfaces, wavy surfaces (characterised for having an $ES < 0.35$) and Gaussian-PSD surfaces, as they might need extra parameters such as ES or Λ_s. Furthermore, in another contribution by Flack in [34], it is found that Rz is an important parameter to determine the onset for the transitionally rough regime. On the other hand, regarding the characterisation of the complete transitionally rough regime there is still a huge work to do as mapping this whole regime is very difficult to accomplish experimentally. A study of the effect of the sign of skewness on drag and flow separation was performed by Flack *et al.* [21], showing that positive skewed surfaces increase pressure drag, mainly due to local flow separation behind roughness peaks. In [20], a long wavelength filter is applied to remove the effects of waviness or undulations that do not add to frictional drag but affect surface statistics. The roughness Taylor microscale is used as the cut-off frequency

as this parameter accounts for the smallest size of the elements contributing to frictional drag. A small improvement is achieved, but the non-filtered formula is still robust and valid with a considerable confidence level, and thus it can be still applied.

Bons [17, 22] dedicated a series of papers to characterise flows on real turbine applications, focusing on the effect of surface roughness on skin friction (c_f) and heat transfer (based on Strouhal number, St), among other phenomena such as freestream turbulence or pressure gradient. Bons demonstrated the higher effect of surface roughness on skin friction than on heat transfer, being the effect on the former four times larger than on the latter. In [17], Bons performs a comparison of the correlation degree of several roughness parameters, including Λ_s, α_{rms} or S_w/S (Total wetted area to smooth area ratio), validating the results with skin friction and heat transfer calculations using directly the equivalent sandgrain parameter, k_s. The parameter Λ_s was adapted to compute it in a discrete way by taking several 2D measurements for the whole 3D domain. This coefficient was found to correlate well with k_s in the fully rough domain using a logarithmic fitting ($R^2 = 0.899$), however it clearly under-predicted c_f in the transitionally rough domain. α_{rms} was also presented, firstly introduced by Acharya [31], as a serious candidate to predict surface roughness in real turbine applications, resulting to have in this study the highest correlation degree ($R^2 = 0.958$), using a 2nd order polynomial fitting. This parameter can be easily measure in real turbine roughness, however it is highly influenced by measuring tool precision. The presence of 90° angles in combination with a small distance between roughness elements can generate big errors and lead to a wrong characterisation of the surface. This limits the use of α_{rms} to fairly uniform roughness and only in the range of $0.5 < k/\theta < 3.0$, being θ the boundary layer momentum thickness, and k being Rz. A α_{rms} correlation needs to be further developed and validated, and so at the moment it is just presented as a potential candidate. In [22], Bons gives further explanation of the procedure to get Λ_s from discrete 2D measurements and the algorithm to characterise full 3D rough surfaces. He then states that the average streamwise forward-facing surface angle, $\overline{\alpha_f}$ and Λ_s are geometrically related, and thus they should share the same degree of k_s correlation. Note that, it is also demonstrated from this work that $\overline{\alpha_f}$ and α_{rms} are mainly linear correlated. Based on Bons [17] and Acharya [31] conclusions, it can be stated that correlations using $\overline{\alpha_f}$ or α_{rms} are expected to provide a high correlation degree as demonstrated for α_{rms}, with the significant advantage of an easier computation with respect to Λ_s.

All the previous research is dedicated to find correlations based on experimental methods, allowing to retrieve the big picture of roughness effects. Local and lower scale effects produced by surface roughness are not captured by experimental methods, and so this is where accurate computational methods, such as Direct Numerical Simulation (DNS) are required to have a detailed representation of the roughness features.

Thakkar *et al.* [28] and Forooghi *et al.* [35] both have performed studies in consecutive years including the use of DNS to find an universal equivalent sandgrain correlation. Thakkar *et al.* designed 17 different irregular rough surfaces in order to apply a DNS procedure at a friction Reynolds number ($\mathrm{Re}_\tau = u_\tau c/\nu$) of 180, keeping the roughness Reynolds number, k_s^+ or k^+, in the transitionally rough regime ($k_s^+ = 30$), to determine the separate effect of the roughness characteristics in the flow features. In this way, the effects of main roughness parameters discussed through literature (λ, s_k, Rq) together with the flow texture ratio (accounts for anisotropy effects comparing the streamwise to spanwise arrangement of the roughness elements) are studied and then ranked based on their correlation contribution to fit the roughness function and peak Turbulent Kinetic Energy (TKE). Conclusions from this study suggest that surface roughness correlations must include at least one slope related parameter (λ, Λ_s or ES), skewness and a roughness height scale, such as Rq or Rz. Regarding the fitting with ΔU^+, Thakkar *et al.* rank the parameters (from more to less importance) as solidity, flow texture parameter, rms roughness height and skewness. When looking at the peak TKE, the order changes, putting first the mean local slope angle, then the skewness and finally the rms roughness height and effective slope. The fitting formulas used are of different nature and adapted to find the best fitting for each parameter. [28] assumes the extrapolation of the results for surfaces in the fully rough domain and suggest a verification of this. Forooghi *et al.* [35] designed a total of 38 rough surfaces, all of them in the fully rough domain by keeping the rms roughness height parameter constant. Effective slope, skewness and kurtosis where varied inside typical ranges verified through literature, and an extra parameter is introduced in the study to account for the distribution of the roughness element size (Δ), meaning when $\Delta \to 0$ all roughness elements are identical, feature that is far from real 3D random roughness. Again a DNS procedure, in this case with friction Reynolds number equal to 500. Forooghi *et al.* conclude that the best fitting includes the effect of the ES and the s_k, with some improvement when including Δ, thus in order to simplify industrial application, a correlation with just s_k and ES is desirable. It is also suggested that in order to scale roughness height, Rz should be used in this case, although in this study it is assumed to be directly proportional to Rq. The correlation proposed is only limited for cases of $\Delta = 0$ and $s_k > 0.7$.

A large set of parameters to describe surface roughness has been presented through this section. As previously commented, at first glance, each work by each author collapse into very different correlations, thus generating a wide range of study trends in this field. Gilge *et al.* [7] performed surface roughness measurements on a set of blades of different stages of real high-pressure compressors after 20,000 life operational cycles. This work provides with the required input experimental measurements to perform a potential validation of a numerical implementation of real surface roughness in axial compressors blades. The experimental measurements from this study can be accessed and thus used in further investigations in this topic, for example to analyse the effect and trends of other parameters that are not taken into account in this study, such as skewness, kurtosis or slope. Results show a large size of the roughness elements at the

leading edge in the first compressor stages. The increased roughness is produced by several mechanisms, but mainly due to impacts, causing round depressions, and/or depositions. A high density of anisotropic asperities is found again at the first stages of the compressor, causing a higher equivalent sandgrain, but without showing an increase in the roughness height. This supports the conclusions of most of the authors mentioned in this review of having to implement more advanced surface roughness parameters to account more accurately for anisotropy of the roughness elements, and thus being closer to a real random 3D surface roughness. Correlations using s_k [10], Δ_s and α_{rms} in combination with a roughness height scale (Ra, Rq and Rz) have been discussed to be used as potential representations of roughness to be used in this Thesis. This set of parameters has been also supported by means of powerful DNS work. Summarizing the main conclusions, it has been shown that s_k provides a very effective modeling of the type of the roughness in terms of impacts (valleys) and fouling (peaks), mechanisms that really influence drag production [21]. Moreover, the slope is also key in the characterisation of the effect of roughness on the flow features as it will provide how steep the peaks/valleys are, and thus the amount of local deflection of the flow at the asperities. Slope related parameters are directly linked between each other, therefore meaning that including only one parameter of this type should be enough to characterise this roughness feature. With all this said, Equation 2.14 [35] is chosen as the most representative correlation to be applied for the case presented in this study. This decision is done based on all the previous evidence provided during this section, and being aware of the simplifications that this model carries, as a DNS with a full representation of a 3D random surface roughness is not considered due to its huge time cost and the time limitations of this study.

$$\begin{aligned} k_s &= Rz\, F(s_k)\, G(ES) \\ F(s_k) &= 0.67 s_k^2 + 0.93 s_k + 1.3 \\ G(ES) &= 1.07(1 - e^{-3.5ES}) \end{aligned} \tag{2.14}$$

2.2. Aeroelasticity in turbomachinery

The pursuit of lighter engines and improved fuel efficiency has led to the design of engines with fewer compressor stages and slender blades. While this design approach achieves weight reduction and increased pressure gradients, it also introduces more flexible blades, influencing the aeroelastic stability of the components [36]. One dangerous phenomenon associated with this is flutter, a self-excited and self-sustained aeroelastic instability that is prone to occur when long and slim blades are subjected to aggressive loading. Flutter has been a subject of research for several decades due to its complexity, as there is currently no reliable predictive method to anticipate its occurrence [37].

Despite meticulous design and safety considerations, compressors may operate closer to

their stability limits than intended. Transient operation, wear, partial component failure, and engine control issues can push the compressor towards these limits [38]. Flutter is a blade-specific phenomenon, strictly linked to the blade's eigenmode. It initiates from an initial blade displacement and exhibits exponentially growing vibration amplitudes. The vibration can be stopped either by structural failure or nonlinear effects that lead to limit cycle oscillations [38].

The structural integrity of rotating parts is crucial for the reliable operation of a power plant, particularly in jet engines. Vibration-induced fatigue failure of rotor blades poses a significant concern for designers. Surprisingly, vibratory failures can occur during the final test phases, even when analytical predictions and rig testing have not indicated any problems [39]. Consequently, flutter assessment remains a critical aspect driven by safety and economic considerations. While 90 percent of potential high-cycle fatigue issues are typically detected during engine development, addressing the remaining 10 percent, which represents a significant portion of the overall engine development costs, is essential [37, 40].

Design engineers strive to ensure aeroelastic stability across a wide range of operating conditions, aiming for free-flutter operation of turbomachines. Achieving this goal requires an understanding of the complex interactions between fluid flow and blade vibrations [37]. Furthermore, Surface roughness is known to be a major factor of performance decrease in turbomachines. There exist some studies aimed to check roughness effects in generic airfoils [41] or wind turbine blades [42], concluding that roughness can either improve the stability of the system or have a small, almost negligible, negative effect on it, respectively. However, its influence on the aeroelastic stability of compressor or turbine blades has not been studied in depth.

Collar's triangle, displayed in Figure 2.7, provides with a schematical representation of the main forces involved in aeroelasticity and aeromechanics. Elastic, inertial and aerodynamic forces interact between each other leading to different phenomena such as static aeroelasticity, mechanical vibrations, stability and control, and dynamic aeroelasticity. It is the last one, the one with the highest value for this thesis, as it is the interaction of the three set of forces the one leading to flutter.

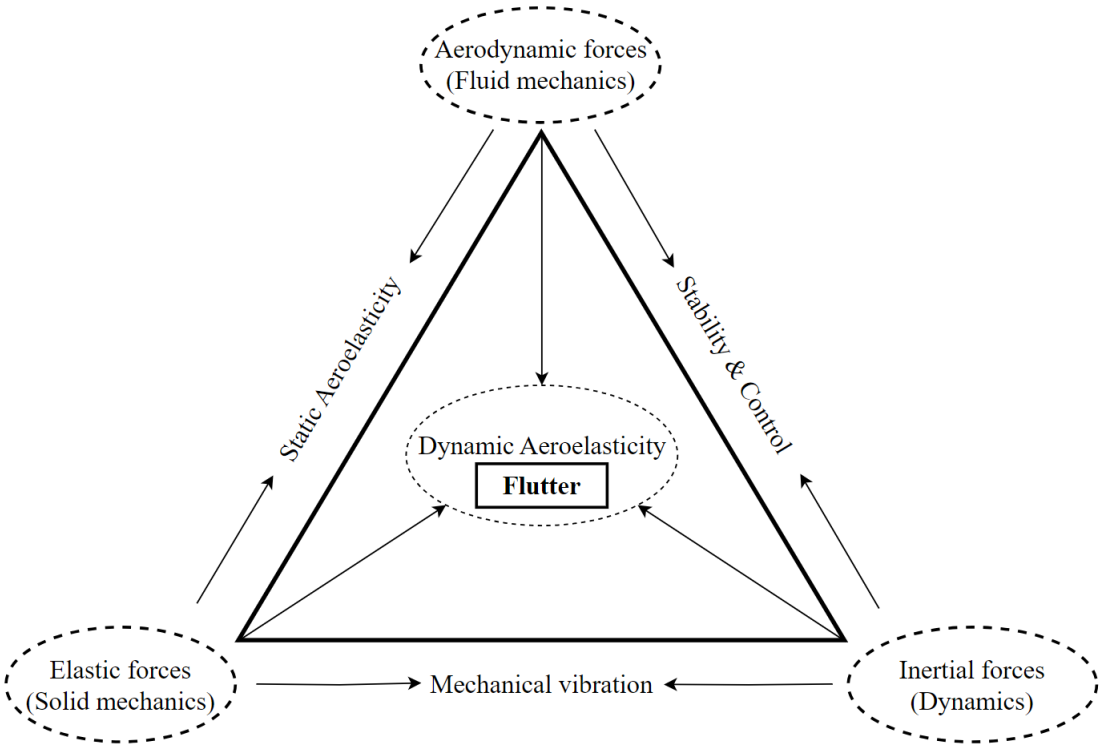

Fig. 2.7. Collar's triangle of forces [43].

Collar's triangle can be expressed mathematically as shown in Equation 2.15. In the Left Hand Side (LHS) of the equation, the structural components are gathered (M_{Struct}, C_{Struct} and K_{Struct}), while at the Right Hand Side (RHS), the aerodynamic forces are represented by $F_{\text{Aero}}(X, \dot{X}, t)$.

$$[M_{\text{Struct}}]\{\ddot{X}\} + [C_{\text{Struct}}]\{\dot{X}\} + [K_{\text{Struct}}]\{X\} = \left\{F_{\text{Aero}}(X, \dot{X}, t)\right\} \tag{2.15}$$

Likewise, the aerodynamic forces can be separated into two main contributions (Equation 2.16), $F_{\text{Exc}}(t)$ corresponding to the unsteady forcing conditions generated by the flow (wakes, potential field, shock waves...), and $F_{\text{Coupled}}(X, \dot{X}, t)$, representing the contribution of the movement (velocity and displacement) of the blades.

$$\left\{F_{\text{Aero}}(X, \dot{X}, t)\right\} = \{F_{\text{Exc}}(t)\} + \{F_{\text{Coupled}}(X, \dot{X}, t)\} \tag{2.16}$$

The aerodynamic coupled force can be moved to the LHS, in terms of an aerodynamic damping contribution, C_{Aero} and an aerodynamic stiffness term, K_{Aero}. The resultant form is displayed in Equation 2.17.

$$[M_{\text{Struct}}]\{\ddot{X}\} + [C_{\text{Struct}} + C_{\text{Aero}}]\{\dot{X}\} + [K_{\text{Struct}} + K_{\text{Aero}}]\{X\} = \{F_{\text{Exc}}(t)\} \tag{2.17}$$

Applying then the transformation shown in Equation 2.18, coming from solving the eigenvalue problem, the equation can be expressed in the frequency domain (Equation 2.19). The oscillation frequency of the system is represented by ω, and the mode shape is introduced by $\hat{X}$. Both the mode shape and frequency are computed performing a modal analysis solving for the undamped equation of motion.

$$\{X\} = \{\hat{X}\} \cdot e^{i\omega t} \tag{2.18}$$

$$\left[-M_{\text{Struct}}\omega^2 + [C_{\text{Struct}} + C_{\text{Aero}}]\,\omega i + [K_{\text{Struct}} + K_{\text{Aero}}]\right]\{\hat{X}\} = \left\{\hat{F}_{\text{Exc}}\right\} \tag{2.19}$$

Finally, in order to solve for the aerodynamic damping, the excitation force is removed, resulting in the homogeneous equation shown in Equation 2.20. This is done as in the context of flutter, only the aerodynamic forces generated by the motion of the blade are significant.

$$\left[-M_{\text{Struct}}\omega^2 + [C_{\text{Aero}}]\,\omega i + [K_{\text{Struct}} + K_{\text{Aero}}]\right]\{\hat{X}\} = 0 \tag{2.20}$$

The unsteady aerodynamics, C_{Aero} and K_{Aero}, are computed using the Travelling Wave Mode (TWM). In this scenario, the oscillation takes place simultaneously in all the blades, following a specific mode, and is analyzed by considering one blade at a time (uncoupled). This approach involves solving the problem using a combination of cosine and sine standing waves in a harmonic manner. As a result, the unsteady pressure is characterized in terms of frequency or cyclic space, using both amplitude and phase information. The unsteady pressure field can be also computed using the so-called influence coefficients, however this is out of the scope of thesis and its formulation description is left to the reader, referring to [37, 44].

2.2.1. Static Aeroelasticity

Static aeroelasticity deals with the interaction between the aerodynamic forces and the elastic forces of the structure in consideration. From a steady point of view, fluid forces produce stresses and deformation on the structures inside the flow field without generating vibrations. From a turbomachinery point of view, blades are exposed not only to the air flow field but also to rotational velocity having to deal with centrifugal loads. This steady deformation and stress state is of great importance as structures will differ from their initial or design state when

running the machine. Moreover, turbomachines in aeroengines may withstand a large range of operating conditions, thus changing this steady deformation state in the internal structures. These two issues are the reason of the necessity of predicting accurately the static aeroelastic behavior, as small changes in this state may generate greater effects on the aerodynamic field or the stability of the most sensitive structures, such as compressor or fan blades.

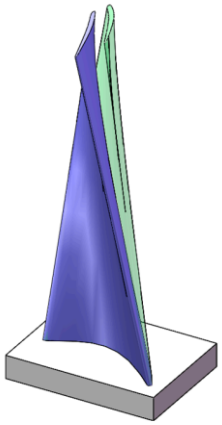

Fig. 2.8. Example of cold (blue) and hot (green) blade states due to static aeroelastic interaction [45].

2.2.2. Dynamic Aeroelasticity

Dynamic aeroelasticity involves all the phenomena regarding the interaction between airflow and structure in the unsteady regime, thus leading to the onset of vibrations. These vibrations are also known as flow induced vibrations and can be classified into different families depending on its nature, characteristics or relation with the rotational velocity. Holzinger *et al.* [38] provides a very clear classification of the different categories as shown in Figure 2.9.

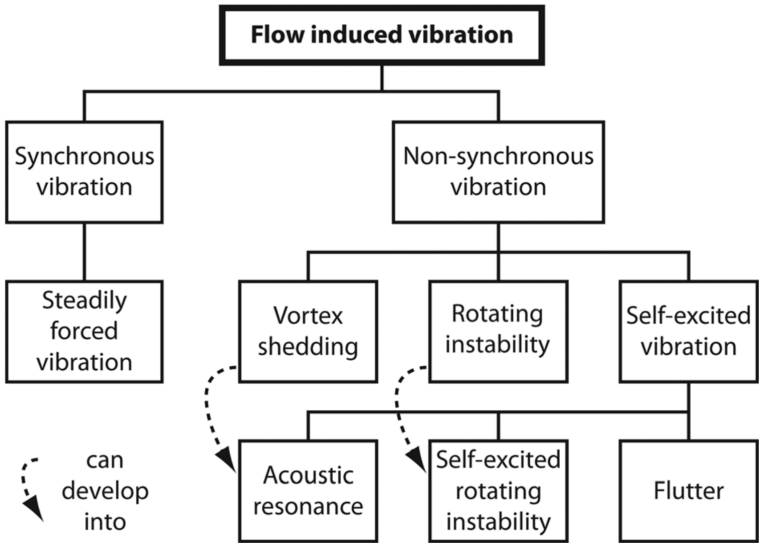

Fig. 2.9. Flow Induced Vibrations [38].

Synchronous vibrations refer to vibrations where the frequency of vibration is directly related to the rotational frequency of the machine. Forced vibration is included in this family, as this type of vibrations are encountered when the excitation frequency matches the natural frequency of blade and/or disk. An assessment of the critical or unsafe points is made by applying and analyzing the characteristic Campbell diagram of the system together with the composition of the Zigzag Excitation Line in Nodal Diameter vs. Frequency (ZZENF) diagram. With these tools, the designer can check for possible resonance crossing as well as potential compatibility between mode shape and engine order. Engine order excitation can be divided in two major subgroups. Low Engine Order (LEO) excitation are generated by non-uniform flow conditions (gusts, blocked burner, ground vortex ingestion...) and structural sources, creating a mistuned state. On the other hand, high engine order excitation are produced by upstream or downstream stator blade rows that create wakes and potential fields, respectively, leading to engine order excitation proportional to the number of blades.

On the contrary, Non-Synchronous Vibrations (NSVs) occur at vibration frequencies that do not match integer values of the rotational velocity. The prediction of this vibration phenomena is more challenging than that for synchronous vibrations, which is why their hazard level is also much higher. Following the diagram presented in Figure 2.9, three major groups are included in NSVs: vortex shedding, rotating instabilities and self-excited vibrations.

- Vortex shedding and acoustic resonance [38, 46–48]: Vortex shedding occurs when the flow separates from the surface, creating alternating vortices. These vortices can induce vibrations and oscillations in nearby objects or structures. The shedding frequency depends on factors such as the flow velocity, geometry of the object, and fluid properties. Following the diagram in Figure 2.9, vortex shedding can develop into acoustic resonance

self-excited vibrations. Acoustic resonance is a phenomenon where mechanical structures experience high-level vibrations due to pressure fluctuations caused by acoustic waves. It occurs when the frequency of the acoustic wave matches the natural frequency of the structure or a resonant frequency determined by its geometry. This resonance leads to amplification of vibrations, potentially causing structural damage or inefficiencies in systems. Acoustic resonance can be triggered by factors such as fluid flow, vortex shedding, or the presence of cavities or resonant chambers.

- (Self-excited) Rotating instabilities and rotating stall [38, 46, 47]: Rotating instabilities manifest in turbomachines, particularly when operating at high loaded conditions and significant tip or hub clearances. These instabilities arise from a single blade row and exhibit significant pressure fluctuations at approximately half the blade passing frequency. When one of the aerodynamic modes of the rotating instability locks onto a blade eigenmode, there is a sudden increase in vibration amplitude, transitioning from forced to self-excited vibration. One well-known form of rotating flow instability is rotating stall. It occurs when the incidence angle of a stage increases, leading to boundary separation at specific circumferential positions overloading one adjacent blade while unloading the other. This establishes a rotating stall cell, revolving at roughly half the rotor speed.

2.2.3. Flutter

Flutter encompasses a range of self-excited blade vibrations observed in compressor rotors, characterized by sustained oscillations driven by the interaction of aerodynamic forces, elastic response, and inertia forces within the blade row. It is specifically connected to the blade's eigenmode, occurring solely at its eigenfrequency without any vibrations below or above. Flutter initiates from an initial blade displacement, leading to exponentially growing vibration amplitudes. For flutter to occur, the energy input from fluid motion to the blade exceeds the dissipation-energy provided by mechanical damping.

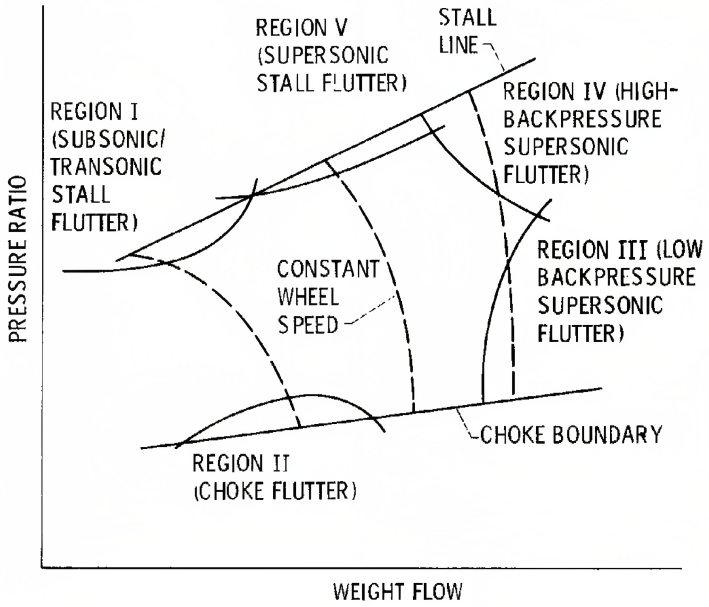

Fig. 2.10. Typical flutter Boundaries on compressor map [49].

- Choke Flutter (Region II) [49–51]: It occurs near the choke line of the compressor map at low rotational speeds, as can be observed in Figure 2.10. This is when the compressor is operating at large mass flow rate and low pressure ratio, leading to a strong shock in the blade-to-blade channel. Choke flutter is commonly seen at small positive or negative angles of incidence, with no flow separation but evidence of partial choking in the cascade passage. The frequency of choke flutter is often close to, but not necessarily equal to, a blade's natural frequency, specifically the first bending mode. The steady flow is subsonic before and after the blade row but becomes supersonic within the blade-to-blade channel. The shock extends from the trailing-edge of the suction side to the pressure side, causing oscillations between neighboring airfoils due to airfoil vibration and modification of the throat area. While less common than other compressor flutter types, choke flutter primarily affects the middle and rear compressor stages. The precise mechanism underlying this instability is not fully understood, but it may involve a passage resonance phenomenon in conjunction with marginal aerodynamic damping.

- Stall Flutter (Regions I and V) [49, 50, 52]: Stall or separated-flow flutter occurs near the stall line of the compressor map, meaning at high loading conditions, and lower mass flow rates. It was the most commonly observed flutter instability prevalent in subsonic and transonic applications before the advent of high-tip-speed fans. Depending on the rotational speed at which the machine is running, it can be classified in subsonic, at part speeds, or supersonic, at higher tip velocities. It have been observed to develop at large positive incidence angles on the suction surface of the blade during part of the oscillatory cycle. At near-design speeds, fans operating at supersonic tip Mach numbers may experience supersonic stalled flutter at high pressure ratios. This type of flutter is believed to be caused by the movement of a strong passage shock and boundary layer separation.

Unlike classical flutter, stall flutter does not rely on elastic or aerodynamic coupling between modes or phase lag. Instead, the nonlinear aerodynamic forces and moments play a crucial role in this instability, leading to the separation of airflow from the airfoil.

- High/Low back pressure supersonic flutter (Regions III and IV) [39, 53–55]: These two flutter regions are encountered at maximum rotational speed line. While high back pressure is found in the range between the operating and stall lines, low back pressure is prone to occur in between the operating line and the choke boundary. Differences appear on the loading conditions and mechanisms leading to the onset of flutter. At low back pressure, the flow remains supersonic and attached, being the reduced frequency, nodal diameter, shock location and mach number its governing parameters. On the other hand, high back pressure supersonic flutter is typically marked by the presence of an intense shock wave within the flow passage, in combination with boundary layer separation.

- Classical Flutter [50, 56, 57]: In classical flutter, the flow remains attached to the blade, distinguishing it from other instabilities. It is not related to any of the above regions. Flutter occurs when the attached flow experiences linearly varying aerodynamic forces with angles of attack. The instability arises from the phase lag between aerodynamic forces and blade displacements. Vortical and acoustic waves, as well as neighboring airfoil interactions, contribute to this phase lag. This type of flutter is more prevalent in rotorcraft applications. In turbine and compressor blisks, aerodynamic damping from the surrounding fluid plays a significant role due to minimal blade-disk friction and limited material damping.

Blade-disk interaction

Vibration modes in turbomachines can be divided mainly in rotor and disk modes, with their corresponding interaction between them. Figure 2.11 shows their common shapes. Blade isolated modes are usually classified as First Bending Mode (1B), First Torsion Mode (1T), Second Bending Mode (2B), etc, and their respective combinations. Depending also in the geometry of the blade, i.e. its design complexity, the mode shapes may differ from the classical ones. Regarding the disk, the modes are dependent on the Nodal Diameter (ND) and Nodal Circle (NCl). However, in axial turbomachines, it is the nodal diameter shapes the ones leading the behavior of the system.

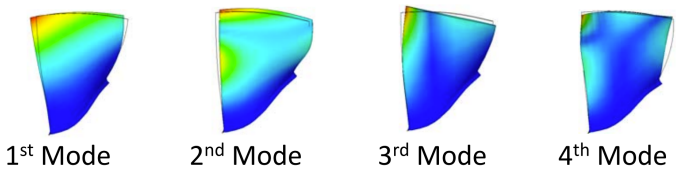

(a) Blade Modes

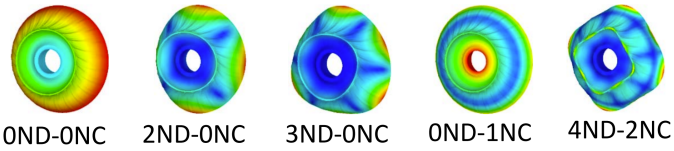

(b) Disk Modes

Fig. 2.11. Typical modes of vibration in turbomachinery blades and disks [44]

Figure 2.12 displays a generalisation of the blade and disk vibration frequency coupling as a function of the nodal diameter of the machine. In this sense, two main regions are identified corresponding to blade dominated or disk dominated as well as a veering or transition region. Blade alone model displays a constant natural frequency no matter the ND excitation, while the opposite happens for the disk modes, suffering a stiffening effect as the ND increases. Within this diagram, the excitation frequency can be also included to relate it to the blade-disk modes, in order to perform a further forced response analysis of the system. However, a forced response study is not in the scope of this project so its description is not included in this report.

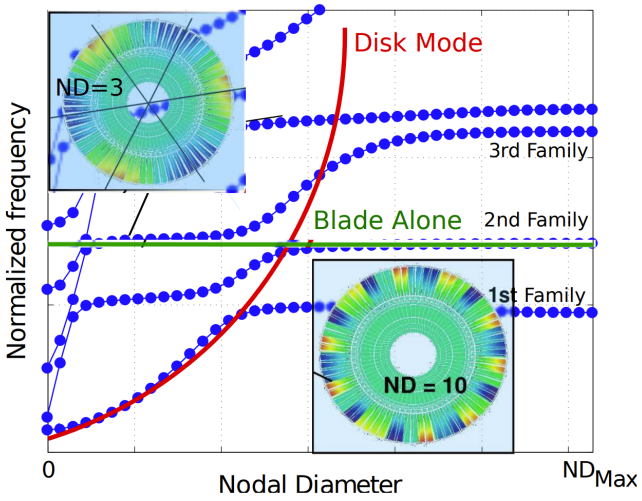

Fig. 2.12. Representation of the blade-disk natural frequencies with respect to the nodal diameter [50].

Nodal diameters are the predominant modes in axial turbomachines. As sketched in Figure 2.13, ND mode shapes produce sequential sectors with positive and negative displacements

separated by the actual nodal diameters, where the deformation remains constant and equal to zero. The total number of nodal diameters in a disk or blade-disk assembly is given by Equations 2.21 and 2.22, depending if the total number of blades is even or odd, respectively:

$$ND = \pm\frac{N_{\text{Blades}}}{2} \tag{2.21}$$

$$ND = \pm\frac{(N_{\text{Blades}} - 1)}{2} \tag{2.22}$$

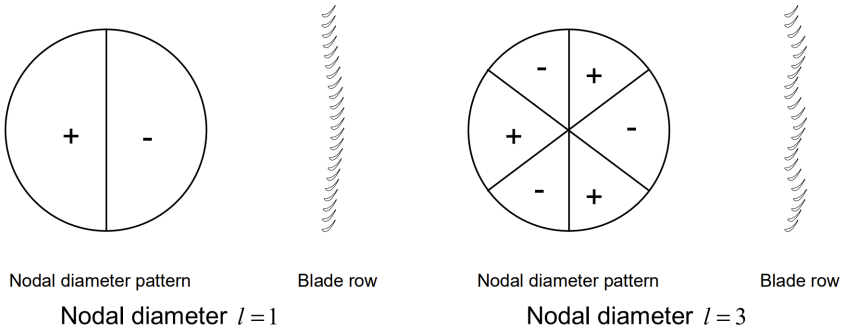

Fig. 2.13. Nodal Diameter sketch [37].

In terms of flutter analysis, the computation of the nodal diameter of interest is crucial. The reason of this is link between the nodal diameter and the relative movement of the blade displacements with respect to the rotational velocity. This relative movement, or shift in the vibration phase is called travelling wave, and depending on its direction with respect to the machine rotation can be of a forward nature (FTW) or backward behaviour (BTW). With this in mind, the concept of Interblade Phase Angle (IBPA), or σ arises. IBPA determines the phase shift between the neighboring blades, as a function of the ND and total number of blades, as shown in Equation 2.23:

$$IBPA = \sigma = \frac{2\pi ND}{N_{\text{Blades}}} \tag{2.23}$$

The main assumption behind the IBPA and the travelling wave relies on the hypothesis of a tuned system. A tuned system is characterized by the premise that all the blades are exactly equal, without any differences in terms of mass or shape. However, in reality, this is impossible to achieve as manufacturing tolerances cannot be avoided, thus providing the system with a certain degree of mistuning. The tuned system assumption is valid as long as this mistuning level is kept low and no additional or intentional mistuning is added to the structure.

Reduced Frequency

Reduced frequency is considered as one of the main parameters to assess and predict flutter. There is a common agreement in literature in which a reduced frequency region where a risk of flutter exists, Flutter is developed at low reduced frequency values ranging from 0.3 to 0.7 [39] or even 1 [37]. This concludes that mainly flutter is produced either at low natural frequencies or at high velocities, also taking into account the geometry of the structure. Reduced frequency is defined as in Equation 2.24:

$$k_{red} = \frac{\omega \cdot c}{U_{\infty,rotor}}, \tag{2.24}$$

where ω refers to the oscillation frequency, c is the blade chord at a reference span location, and $U_{\infty,rotor}$ represents the relative flow velocity at the inlet of the rotor domain.

The link between flutter onset and reduced frequency can be understood by looking at the reduced frequency in a different way, that is as a ratio of time:

$$k_{red} = \frac{c/U_{\infty,rotor}}{2\pi/\omega} = \frac{t_r}{T}, \tag{2.25}$$

where T is the oscillation period, and t_r, the residence time or time that takes for a fluid particle to go through the domain.

With this small reformulation, it is easily shown the link between reduced frequency and flutter. At very low reduced frequencies, $t_r << T$, the flow does not have enough time to adapt to the oscillations of the structure due to its high velocity or to the very low period oscillations. At high reduced frequency, $t_r > T$, the opposite happens, the oscillations feature a very high frequency, thus avoiding the flow to accommodate to the excitation during the residence time. However, at moderate reduced frequencies, this is the range already mentioned ($k_{red} \sim$ 0.3-1), the flow and the oscillations are able to adapt to each other, thus allowing for the self-excitation phenomena.

Aerodynamic damping

Flutter prediction and aeroelastic stability are evaluated thanks to the aerodynamic damping. This aerodynamic damping is computed as the logarithmic decrement, δ as shown in Equation 2.26 [58, 59]:

$$\delta = \frac{W_{\text{cycle}}}{2KE_{\text{ave}}} = 2\pi\zeta, \tag{2.26}$$

where W_{cycle} represents the net work per vibration cycle, KE_{ave} is the average kinetic energy of the blade [58], and ζ stands for the critical aerodynamic damping. This result provides with the necessary information to evaluate the stability of the system. A positive aerodynamic damping value (or work-per-cycle) indicates that the oscillations are damped, and thus there is not risk of flutter. Flutter will occur for negative values of the aerodynamic damping, meaning that the flow is contributing to increase the system instability.

The work-per-cycle is computed as the double integral of the fluid pressure, p, times the vibration velocity of the blade, v, over the surface area, A, during one oscillation period, T (Equation 2.27).

$$W_{\text{cycle}} = \int_{t_0}^{t_0+T} \int_A p\vec{v} \cdot \hat{n} dA dt \tag{2.27}$$

The average kinetic energy is computed based on the oscillation frequency, ω, the modal mass, m and the maximum oscillation amplitude, A_{max} [59]:

$$KE_{\text{ave}} = \frac{1}{2} m \omega^2 A_{\text{max}}^2 \tag{2.28}$$

This definition is not universal and there exists a broad discussion on which representation of the aerodynamic damping shows a better agreement with existing experimental data [37, 44]. Main differences rely on the denominator chosen to normalize the work-per-cycle. Other authors use definitions based on a reference pressure and characteristic lengths. However, for the purpose of this thesis, the definition in Equation 2.26 is chosen, because of the selected normalization with the kinetic energy allowing to have a direct relationship between the motion of the blade and the work-per-cycle.

The computation of the aerodynamic damping is done for each ND. The evaluation of the whole ND domain is required to identify NDs that are more prone to flutter. The final output, in order to characterise the flutter behaviour of the blade row is given by a diagram similar to the one displayed in Figure 2.14, known as aerodynamic damping S-curve:

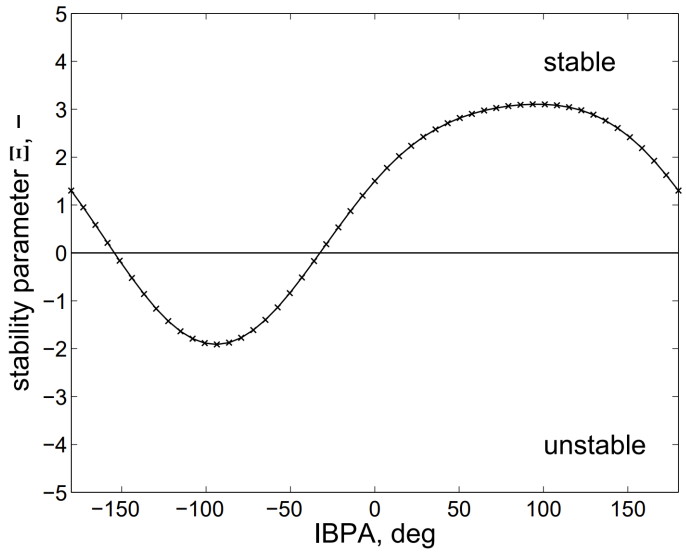

Fig. 2.14. Representation of the aerodynamic damping with respect to the interblade phase angle (or ND) [37].

Mistuning

Mistuning is defined as any aspect of the structure or the aerodynamics of the machine that prevents the system and behavior to be fully symmetric, i.e. infringement of the tuned system assumption. Mistuning can be caused by several reasons, structural or aerodynamic, and depending on its origin, it can be random or intentional. Random or unintended structural mistuning is usually caused by manufacturing tolerances or deterioration of the blades or disk. Surface roughness can be included as some sort of unintended mistuning introducing dissimilarities in the flow. Random mistuning, as its name suggests, cannot be predictable in advance, and thus its effects threaten the integrity of the structures. Its study is of a high interest in order to try to anticipate its effects. The direct effects of structural mistuning have been found in the aeroelastic stability of turbomachines as they directly affect the natural frequency of the structures by the modification of their shape. Intentional mistuning (aerodynamic and/or structural), in combination with an accurate stability study, can be used to avoid flutter onset. Some of the most extended methods to introduce intentional mistuning in the system are the modification of the inflow conditions (IGVs configuration), or the variation of structural features such as blade shape and weight, tip clearances, dampers, etc.

3. METHODOLOGY

The purpose of this chapter is to introduce the concepts concerning the methodology followed in this thesis. It starts by presenting the study case used to carry out the studies. Following that, the chapter is divided into two main sections. The first one aimed to clarify the main concepts behind the implementation of surface roughness in CFX, and the second one intended to show the different modules and setups followed to arrive to the final output of the project.

3.1. Study Case

The numerical study intended for this thesis is performed on the first stage of the VINK. Virtual Integrated Compressor Demonstrator (VINK) is a three-stage, transonic and high efficiency conceptual compressor developed by GKN Aerospace, Swerea IVF and the universities of KTH Royal Institute of Technology, Chalmers University of Technology, and Lund Institute of Technology. The purpose of the VINK project is the development from a clean state of a test case for subsequent optimization and analysis [60]. All the information and files constituting the VINK project, which is an open-source initiative, can be found in the [61] repository and in the reference study by Lejon *et al.* [60].

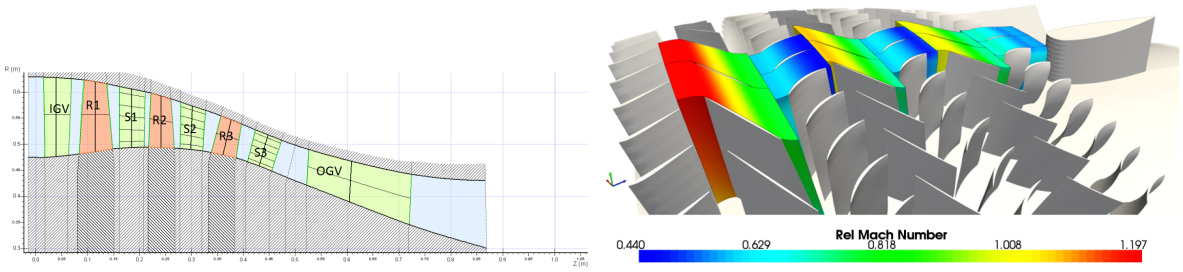

(a) Meridional view

(b) 3D view with relative Mach number

Fig. 3.1. VINK preliminary geometry, composed of a set of IGVs, three stages and a set of OGVs [60].

The baseline geometry for the first stage, shown in Figure 3.1, adopts the name R1S1A. However, the geometry chosen for this study corresponds to a further optimization of the rotor shape named R1S1B. Moreover, in the original design R1S1B, the rotor tip clearance is not

considered, while for the purpose of this thesis it is added. The size of the tip gap considered is 1% of the rotor blade span, following a common rule of thumb. Table 3.1 shows the information regarding the principal dimensions of the compressor stage. The blade material is Titanium alloy Ti-6Al-4V [60].

TABLE 3.1. R1S1B STAGE DIMENSIONS

		Rotor	**Stator**
Span		0.1407 m	0.112 m
True Chord	*Tip*	0.1056 m	0.056 m
	Mid span	0.0987 m	0.055 m
	Hub	0.1040 m	0.051 m
Tip gap		1.3 mm	-
Channel Height		0.142 m	0.112 m
Mean Radius		0.551 m	0.550 m
Blade Count		51	88
Stagger Angle	*Tip*	65.63 deg	27.82 deg
	Mid span	56.45 deg	26.91 deg
	Hub	51.82 deg	22.32 deg

3.2. Roughness & turbulence modeling

The implementation of surface roughness in CFD codes depends on different factors. The main ones rely on the code developer and the turbulence model or the fluid equations to solve (RANS, URANS, LES, DNS, etc.). The desired degree of accuracy of the simulation and time limitations play a very important role in the surface roughness modeling as they do constrain the choice of turbulence model and, therefore, also the implementation of surface roughness.

Regarding DNS, there exist several studies in which surface roughness has been modeled with this method. It presents the most reliable representation of surface roughness as it allows to generate any surface with the desired shape and roughness distribution. But not only that, DNS will be able to solve for the local flow features generated by the smallest scale surface roughness characteristics. This provides enough information to be able to find the most accurate surface roughness correlation, looking at the effect of each parameter separately and being able to compare the results with experimental data if available. Examples of studies with DNS surface roughness modeling are those developed by Thakkar *et al.* [28], Forooghi *et al.* or Vadlamani *et al.* [62], where, in separate investigations, flat plates with different surface roughness distributions were used to understand the local mechanisms due to the interaction between the flow and the asperities. The biggest drawback regarding surface roughness modeling with DNS

is the very high computational cost required for each case, thus being discarded for the thesis here presented.

In the context of CFX, surface roughness modeling is directly related to the selection of the turbulence model. As this project is based on the RANS/URANS equations, the review and analysis will be focused on the turbulence models based on these. The main turbulence models considered for the project were $k-\epsilon$, $k-\omega$ and Shear Stress Transport (SST). These are two-equation turbulence models where the "velocity and length scales are solved using separate transport equations" [63].

- k-ϵ

  The $k-\epsilon$ turbulence model relies on two variables, turbulence kinetic energy (k) and turbulence eddy dissipation (ϵ), which represent the variance of velocity fluctuations and the rate at which these fluctuations dissipate, respectively [63]. Despite known limitations, the $k-\epsilon$ model is robust, widely used, easy to implement, and computationally efficient. It is best suited for fully turbulent flows and is commonly employed in initial iterations, initial screening of designs, and parametric studies. However, it may perform poorly for complex flows involving severe pressure gradients, separation, and strong streamline curvature. Its most significant weakness lies in the lack of sensitivity to adverse pressure gradients [64, 65].

- k-ω

  The $k-\omega$ turbulence model is well-suited for low-Reynolds number computations near walls. It connects turbulence viscosity with turbulence kinetic energy and turbulent frequency (ω), providing increased accuracy and robustness. It allows for a smooth transition from a low-Reynolds number form to a wall function formulation [63]. The $k-\omega$ model performs well in simulations of wall-bounded boundary layers, free shear flows, and low Reynolds number flows. It is especially suitable for complex boundary layer flows involving adverse pressure gradients and separation in applications like external aerodynamics and turbomachinery. However, this model requires high mesh resolution near walls to yield accurate results [64].

- SST

  The SST (Shear Stress Transport) model combines the strengths of the dissipation based and the ω-based models, hence offering improved accuracy. The success of the SST model relies heavily on well-designed blending functions. Nevertheless, the SST model

may still struggle with predicting the onset and extent of flow separation on smooth surfaces. One common issue is the tendency to overpredict eddy viscosity [63, 66]. Despite this limitation, the SST model remains highly recommended for achieving accurate boundary layer simulations, particularly when dealing with adverse pressure gradients [64].

3.2.1. Treatment of rough walls

ANSYS CFX near-wall treatment is based on the concept of wall functions. Wall functions provide the required formulation to model the velocity profile in the different regions of the boundary layer. ANSYS CFX presents two different methods, Scalable Wall Functions and Automatic Wall Treatment, that are suitable when walls are hydraulically smooth. However, in engineering flows, surface roughness significantly impacts the results. Surface roughness leads to increased turbulence production near the wall, causing substantial rises in wall shear stress and wall heat transfer coefficients. Accurately modeling surface roughness effects is essential for precisely predicting near wall flows, especially when considering heat transfer and achieving good agreement with experimental data. Wall roughness disrupts the viscous sublayer, resulting in an downward shift in the logarithmic velocity profile [11]. The downward shift is included in the law of the wall by means of the roughness function, represented by $(-\Delta U^+)$:

$$U^+ = \frac{1}{\kappa} \ln y^+ + B - \Delta U^+ \tag{3.1}$$

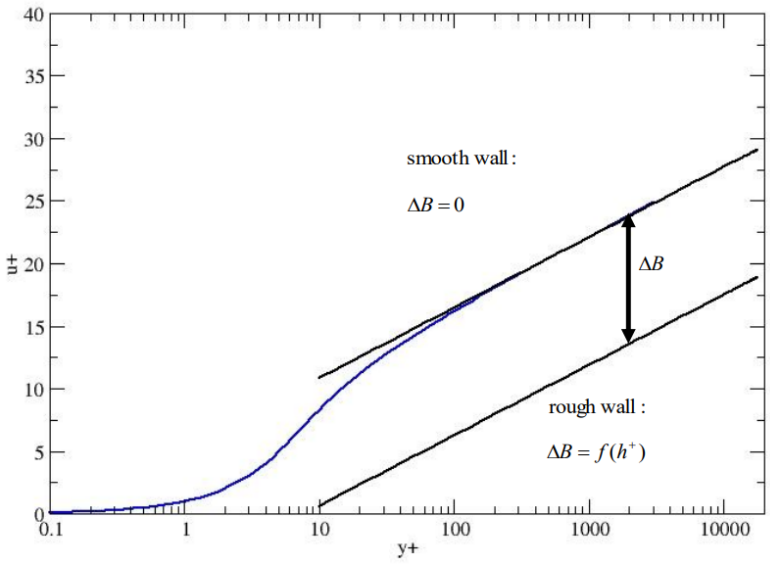

Fig. 3.2. Law of the wall and downward shift due to roughness. ΔB being ΔU^+ [11].

When using sandgrain roughness, the roughness function can be modelled as:

$$\Delta U^+ = \frac{1}{\kappa} \ln\left(1 + 0.3k_s^+\right), \tag{3.2}$$

with k_s^+ being the nondimensional roughness height expressed as:

$$k_s^+ = k_s \frac{u_\tau}{\nu} \tag{3.3}$$

To account for the blockage effect of roughness, it is assumed that it is approximately 50% of its height, so the wall is physically placed at 50% height of the roughness elements as specified in Equation 3.4 [63].

$$y = \max\left(y, k_s/2\right) \tag{3.4}$$

ANSYS CFX presents a modification of the Scalable Wall Functions and Automatic Wall Treatment for the implementation of roughness. Scalable Wall Functions are the default method to be used in conjunction with $k-\epsilon$ models. This method ignores the viscous sublayer and shifts the wall to be above this region by defining a lower bound, in combination with Equation 3.4:

$$y^+ = \max\left(y^*, k_s^+/2, 11.06\right) \tag{3.5}$$

with y^* being the scaled distance from the wall given by:

$$y^* = \frac{u^* \Delta y}{\nu}, \tag{3.6}$$

where Δy is the distance from the wall, and u^* is the alternate velocity scale: $u^* = C_\mu^{1/4} k^{1/2}$, where C_μ is the $k-\epsilon$ model constant, equal to 0.09, and k is the turbulence kinetic energy (TKE). For more details refer to [63].

Automatic Wall Treatment is the default method for ω-based turbulence models, such as $k-\omega$ and SST, among others. Scalable Wall Functions rely on problematic physical assumptions, particularly at lower Reynolds numbers where the neglecting the sublayer in the mass and momentum balance can introduce errors in the displacement thickness. On the other hand, the main concept behind Automatic Wall Treatment is to blend the wall value between the logarithmic and near-wall formulations. This allows for consistent and y^+ insensitive mesh refinement. While the Automatic Wall Treatment performs well for smooth walls and has been extended for rough walls with calibrated coefficients for y^+ and k_s^+, it encounters limitations when dealing with large values of k_s^+. As a result, placing the wall physically at 50% height of the roughness elements is proposed to reduce the blending between the viscous sublayer and logarithmic region, making the viscous sublayer formulation influential only for small values of in the automatic near-wall treatment for rough walls. The blending function formulation is detailed in *Lechner and Menter* [11]. In this report, it is also presented a Scalable Wall Function method

to be used with ω-based turbulence models. The motivation behind this new formulation is the reduction of a limit error that arises for very refined meshes when applying the Automatic Wall Treatment. According to [11], this error is reduced to 1%, decreasing it by a factor of ten when compared to the Automatic Wall Treatment. For the purpose of this project, the Automatic Wall Treatment is selected as the method to apply. This choice has been made due to the fact that the selection Scalable Wall Function method for SST turbulence model was not up-to date in ANSYS CFX leading to errors in the setup file. Some discrepancies arise regarding the formulation of this method between the ANSYS CFX documentation [63] and the *Lechner and Menter* report [11], which is directly referenced in the documentation.

3.3. Flutter Prediction in CFX

Figure 3.3 presents the workflow followed to complete the task of predicting the aerodynamic damping value and check for possible flutter regions.

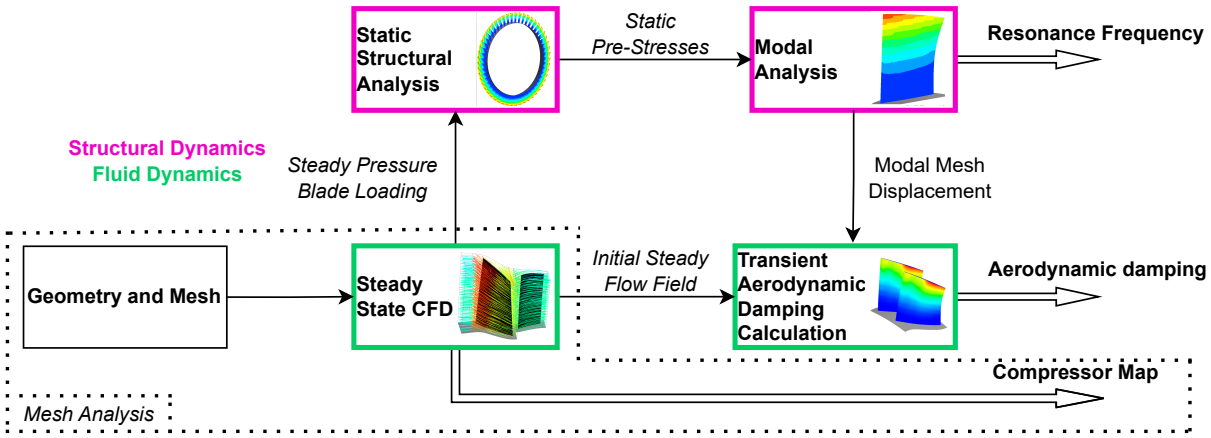

Fig. 3.3. Aerodynamic damping prediction workflow

The process starts by importing the geometry performing the required transformations, such as coordinate frame alignment and stage trimming, so it can be transferred to the mesh generation software. The mesh is created with the desired properties and degree of refinement in terms of overall and local (tip gap) nodes and elements to discretize the geometry. Once the mesh is generated, the setup file is prepared so that a steady-state analysis can be performed. From the steady simulations, the compressor map can be generated, and the Operating Points (OPs) of interest can be evaluated. Moving to the structural dynamics, a static structural analysis and modal analysis (using the pre-stress of the rotational speed and the blade loading of one operating point) are performed in order to get the resonance frequency of the blade and the modal shape. Finally, the transient aerodynamic damping setup can be prepared, importing the modal mesh displacement and the steady flow field coming from the modal analysis, and the steady-state simulations, respectively. Performing a flutter analysis, the aerodynamic damping can be

computed for each nodal diameter and each surface roughness of interest.

All the steps here presented were performed in the ANSYS CFX/Workbench environment with the 2021R2 ANSYS release. See Table 3.2 for the software employed throughout the project.

TABLE 3.2. SOFTWARE EMPLOYED

Stage	**Software**
Geometry	*ANSYS DesignModeler*
Mesh	*ANSYS Turbogrid*
Fluid Dynamics	*ANSYS CFX*
Structural Dynamics	*ANSYS Mechanical*
Post-Processing	*MATLAB, Python*

3.3.1. Geometry and Mesh

The geometry *R1S1B* was generated in the *DesignModeler* environment of ANSYS. The surfaces corresponding to the first stage of the VINK were imported, ending with a complete set that included the rotor and stator blades, and the hub and shroud surfaces. The geometry was aligned to be consistent with the main axes of the machine, i.e. *X - Radial*, *Y - Rotational*, and *Z - Streamwise*:

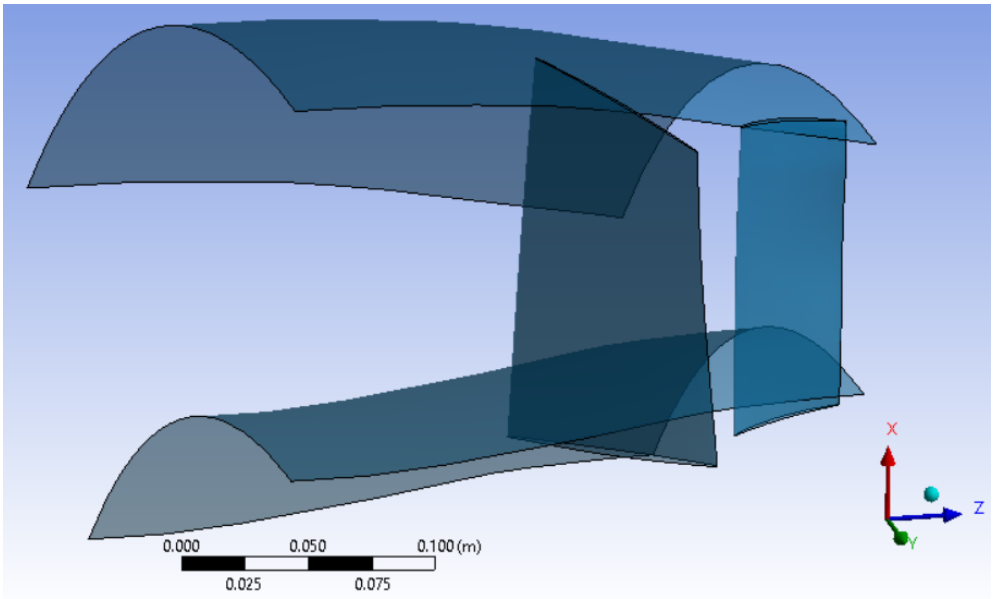

Fig. 3.4. Geometry generation in the *DesignModeler* interface

Mesh generation was done with *Turbogrid*. This software allows for a simple mesh generation specifying the desired mesh parameters in terms of size, distribution or expansion ratios.

In order to allow for a better refinement and mesh control in the rotor, the meshing process was separated between the stator and rotor domain as displayed in Figure 3.5. Both domains share a set of values that remain fixed for all the meshes generated when performing the mesh independence study. The first element offset is controlled by the y^+ value and is set at 2 for all the meshes generated ($Re = 10^6$). This is to be consistent with the selection of the SST turbulence model, allowing to solve for the boundary layer. Moreover, the passage size was always adjusted leaving it proportional to the global mesh size factor. The tip gap region was meshed to always have an expansion rate matching the adjacent passage and shroud element growth rates.

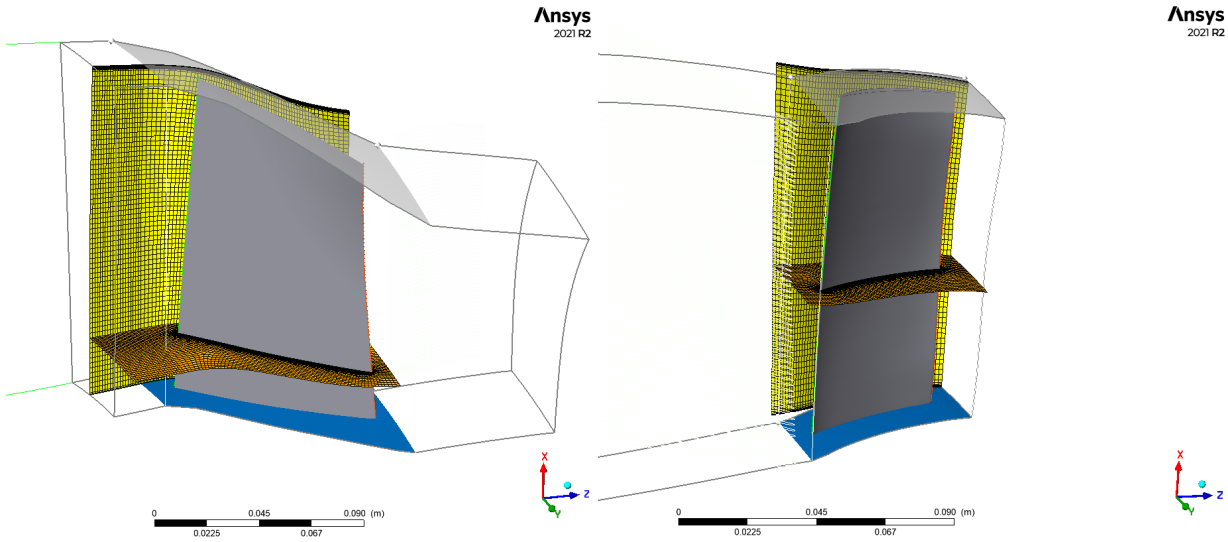

(a) Rotor mesh (b) Stator mesh

Fig. 3.5. Mesh generation in *Turbogrid*

3.3.2. Steady-State setup

The meshes from the rotor and stator were imported, and the boundary conditions were specified. Table 3.3 displays a summary with the principal boundary conditions implemented in the model. Regarding the boundary conditions for the total pressure and flow angle distributions, second order polynomial fits were used as suggested by the VINK developers [61]. Flow angles, total pressure and total temperature are defined in the stationary reference frame.

TABLE 3.3. STEADY STATE BOUNDARY CONDITIONS

Total Pressure at rotor inlet	0 span	47.6945 kPa
	50 span	47.7743 kPa
	100 span	47.8160 kPa
Total Temperature at rotor inlet		282.4 K
Flow angle at rotor inlet[a]	0 span	0 deg
	50 span	-10 deg
	100 span	-18 deg
Rotational Velocity		6242 rpm

[a]Positive in the direction opposite to that of the rotational direction of the rotors.

These boundary conditions were applied at the inlet domain. This section was included in order to have a better application of the boundary conditions by letting the flow develop with the desired properties before entering the rotor domain. As the length of this area is short enough, it did not influence the results and allowed to have a better and faster convergence of the results, when compared to the same cases with only the rotor and stator domains. At the stator outlet region, a value for the static pressure was specified, depending on the operating point of interest. In order to determine which point corresponded to the Peak Efficiency (PE), the compressor map was built for a defined range of outlet static pressures. Moreover, surface roughness was specified in terms of the sandgrain roughness height, k_s, on the rotor blade, after selecting the *Rough Wall* boundary condition. In this implementation of surface roughness, an uniformly distributed roughness height is assumed at every blade location, as well as for each blade in the stage, hence maintaining the tuned system assumption. Figure 3.6 shows the geometry setup used for all steady-state simulations.

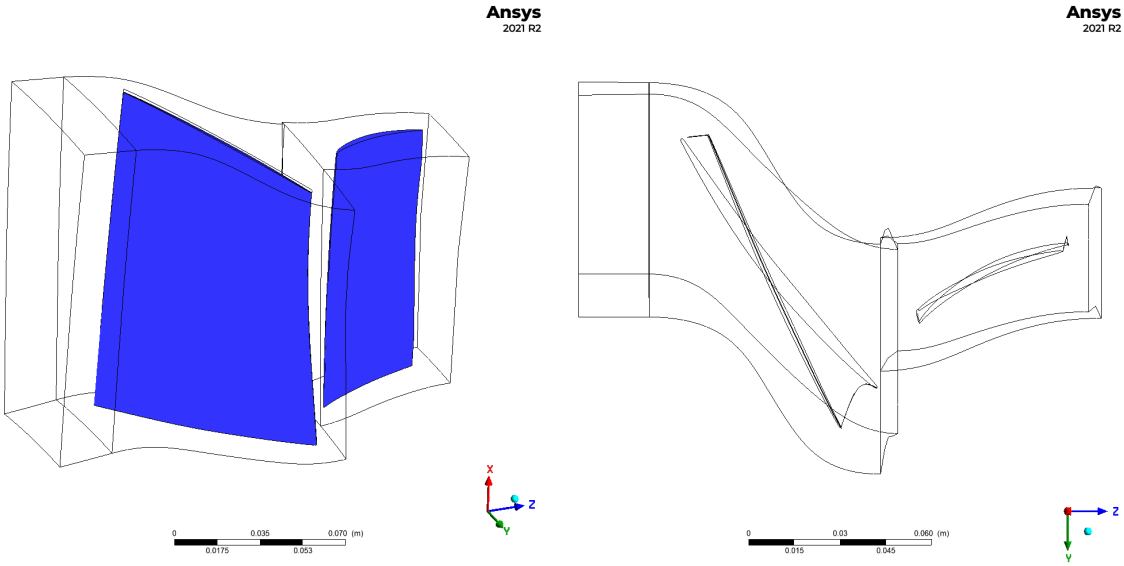

(a) (b)

Fig. 3.6. Steady-state geometry setup in *CFX-Pre*

Regarding the convergence criteria, monitor properties were defined. These included average total pressure at the outlet interface, rotor and stator blade loading, inlet and outlet mass flow rates, total pressure ratio, etc. The cases were considered converged when the monitor variables were stabilized experiencing changes in their values lower than 1% relative to the previous 20 iterations, while the momentum and mass residuals were kept below 1e-5.

3.3.3. Compressor Map & Mesh study

As a result of the steady-state simulations, the compressor map was built for the characteristic speed line of N100. The identification of the compressor map is clue for the further study of surface roughness effects with respect to a specific operating point. In the reference study by Lejon *et al.* [60], all the results presented are computed without including a tip clearance in the rotor. Therefore, there exists the need to recompute the compressor map to see the effect of tip-gap phenomena on the operating range of the compressor stage.

In addition, the compressor map variables (efficiency, pressure ratio and mass flow) can be very dependent on the quality of the mesh. At this point, a mesh independence study is essential in order to be certain that the mesh is not influencing the results.

A large set of meshes with different characteristics was elaborated. The variables that were modified were the global element size, number of tip gap elements or expansion ratios of the elements in the passage. y^+ first element offset was kept constant with a value of 2. Stator mesh, with a size of 470,000 elements, was not modified throughout the study. A total of eight meshes

were generated in the rotor domain. These meshes were evaluated in two different ways, the whole set was computed at the peak efficiency point, while a shorter set of four meshes was selected to build the complete compressor map, as presented in Figure 3.7.

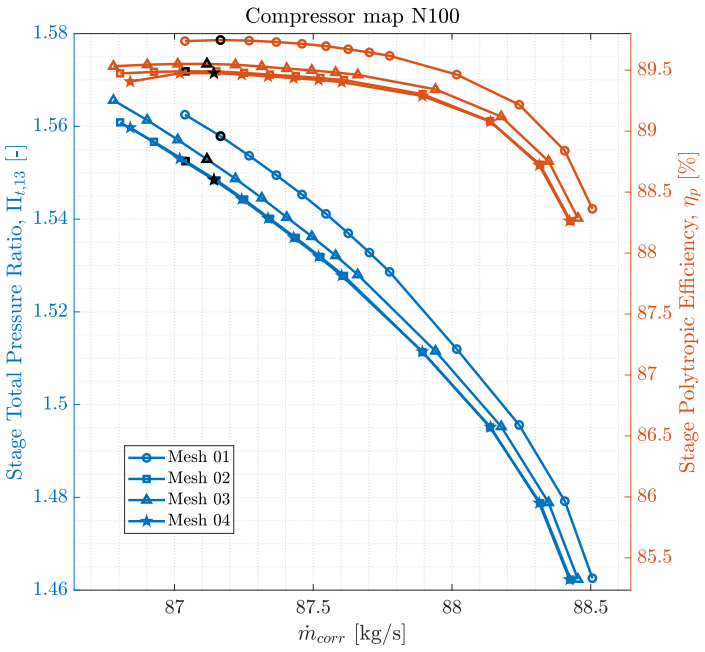

Fig. 3.7. Mesh study with compressor map comparison

TABLE 3.4. ROTOR MESH FEATURES

MeshID	Elements	Tip Elements
01	1,202,000	65
02	902,000	52
03	1,171,000	67
04	767,000	50

Mesh 03 was selected as the reference for evaluating the relative error magnitude, displaying notably stable convergence. First, the results of the Peak Efficiency point revealed that all relative errors remained below 1%. The relative errors were computed not only for the compressor map variables, but also for the blade loading of both the rotor and stator blades. It was concluded that the tip gap region significantly influenced the numerical stability of the simulations, deteriorating the convergence for operating points close to the stall limit. The features of these meshes are summarized in Table 3.4. The differences in the compressor maps were minimal, since the size of the tip gap set a lower limit for the number of nodes, compromising the quality of the mesh for more coarse ones. For the subsequent cases, *Mesh 03* was selected as the final mesh for the rotor domain.

3.3.4. Transient State: Flutter analysis setup

In ANSYS CFX, the procedure for studying blade flutter entails modeling the transient response of a blade row using the Fourier transformation method.

The analysis of transient flows in turbomachines can be computationally demanding due

to the need to model the entire geometry of the turbomachine, which can have varying blade counts in different rows [63]. To mitigate computational costs, a reduced model approach can be adopted using pitch-change methods like Profile Transformation, Time Transformation, or Fourier Transformation.

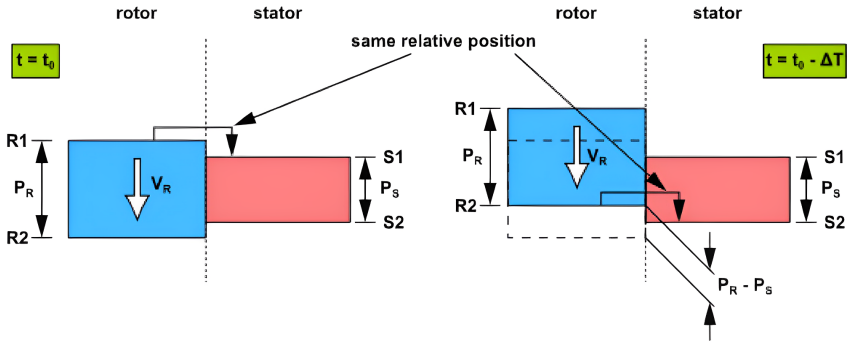

Fig. 3.8. Schematic representation of phase-shifted periodic boundary conditions for Time Transformation method [63].

Both Fourier and Time Transformation methods in ANSYS employ phase-shifted periodic boundary conditions (**??**). The fundamental principle behind this approach is the periodic interaction between pitchwise boundaries at different time instances. Specifically, the Fourier Transformation method directly imposes a phase shift between the rotor domain boundaries for the variables of the problem. By employing temporal Fourier series decomposition (Equation 3.7), the method effectively breaks down the signal into harmonics corresponding to each passage's fundamental frequency, allowing for the reconstruction of the solution at any desired arbitrary time on the periodic boundaries [58, 63].

$$f(t) = \sum_{m=-M}^{M} A_m e^{-j(\omega m t)} \tag{3.7}$$

In ANSYS CFX, the Fourier Transformation method is implemented through a double-passage approach (Figure 3.9), which yields more efficient convergence compared to the single-passage method [63]. The double-passage method involves collecting data at the implicit interface between adjacent passages [58].

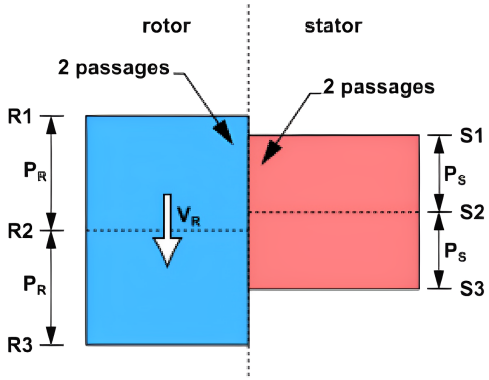

Fig. 3.9. Schematic representation of double passage method [63].

Ensuring adherence to the Geometric Conservation Law (GCL), the mesh motion is specified as a boundary condition. The GCL (Equation 3.8) stipulates that for each control volume, the rate of volume change must precisely balance the net volume swept due to boundary motion [58].

$$\frac{d}{dt_v}\int_{V(t)} dV = \int_S W_j dn_j, \tag{3.8}$$

where W_j denotes the velocity of the control volume boundary.

Figure 3.10 displays the geometry used to carry out the transient flutter analysis cases. The setup just includes two passages of the rotor domain.

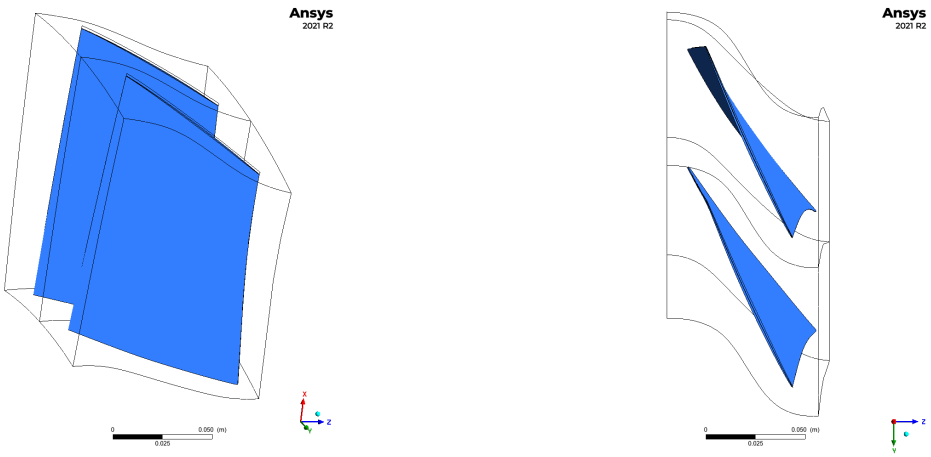

(a) (b)

Fig. 3.10. Transient state geometry setup in *CFX-Pre*

The boundary conditions used to initialize the simulation were extracted from the same locations coming from the steady-state results. In a similar way as for the steady cases, the BCs applied were the total pressure and flow angle distributions at the rotor inlet in the stationary frame, and the average rotor outlet static pressure. Moreover, the mesh displacement, extracted from the modal analysis, was introduced on the rotor blade surface. The mode selected was

the first bending mode. This choice was based on the value of the reduced frequency, k_{red}, for this mode and case. The computed value for k_{red} was 0.53 (f = 319.23 Hz, c = 0.0987 m $U_{\infty,rotor}$ = 372.95 m/s) meaning that this mode presents chances of featuring an unstable region. This clearly increases the interest of studying the effects of surface roughness with this mode, from an aeroelastic perspective.

The last steps for the transient setup concern the specification of the solution control variables. Time period was define as the inverse of the oscillation frequency of the blade. Moreover, the number of timesteps per period was chosen to be an integer of $4\frac{N_{\text{Blades}}}{ND}$ [67]. Total simulation time was controlled with the number of periods per run. This was selected to be 8 periods per run for most of the cases, in order to have a good convergence margin, even though ANSYS documentation [63] states that convergence should be achieved within 4 periods. Regarding the convergence control, a new set of monitor points was defined. In addition to the monitor points defined in the steady-state analysis, the Wall Work Density (WWD), blade torque and work-per-cycle were added. The latter is the main output of these simulations, as after normalizing, it will provide with the aerodynamic damping value, as described in Equation 2.26. An example of the monitoring and convergence control of this variable is given in Figure 3.11. In this figure, the computed work-per-cycle, already normalized to have the critical aerodynamic damping, is shown for both blades in the domain. The convergence criteria used was to have a relative variation of less than a 1% with respect to previous 100 iterations, as well as less than 1% of relative difference between the aerodynamic damping value of blade 0 and blade +1.

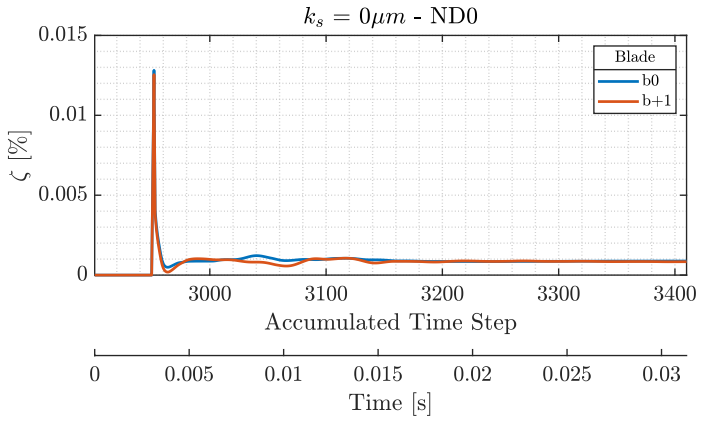

Fig. 3.11. Aerodynamic damping monitor point: Example of convergence control. Smooth case (k_s = 0μm), ND = 0.

Monitoring all these quantities provides with a clear view of the oscillating behavior of the system, as well as being able to check for the mean value representing the steady-state solution. Figure 3.12 displays an example of this with the Blade Loading monitor:

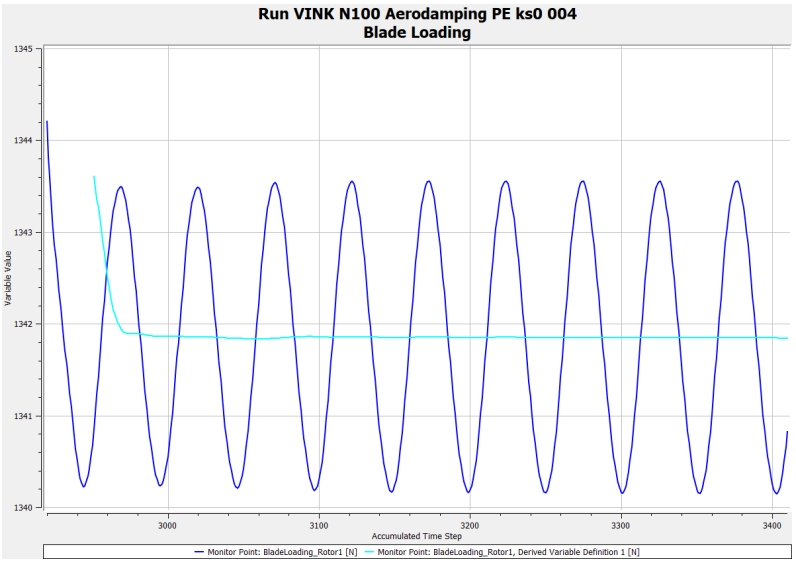

Fig. 3.12. Blade Loading monitor point: Example of convergence control. Smooth case ($k_s = 0\mu m$), ND = 0.

4. RESULTS

This chapter aims to show the main results from the numerical study. It follows the same structure as the methodology section, starting from the steady-state results and then moving into the flutter analysis, showing the final aerodynamic damping S-curve for each sandgrain roughness height value.

4.1. Steady State

This section is aimed to show and explain the main results extracted from the steady-state analysis of the different cases, with and without rough surfaces. It is split into three parts, concerning first the results of the baseline compressor case, following with the presentation of the local flow features of the stage, also for the baseline case, and ending with the identification of the roughness effects on the steady-state behavior of the compressor stage.

4.1.1. Compressor Map

The characterization of the compressor map is essential to progress with the study. Reference results from Lejon *et al.* [60] provide the compressor map at nominal speed, but without considering the tip clearance of the rotor. As a consequence of this, the characteristic speed lines are affected by a shift towards smaller mass flow rates and a smaller operating range [68]. Peak Efficiency (PE), Near Stall (NS), and Near Choke (NC) OPs also change, and they need to be evaluated with the new geometry.

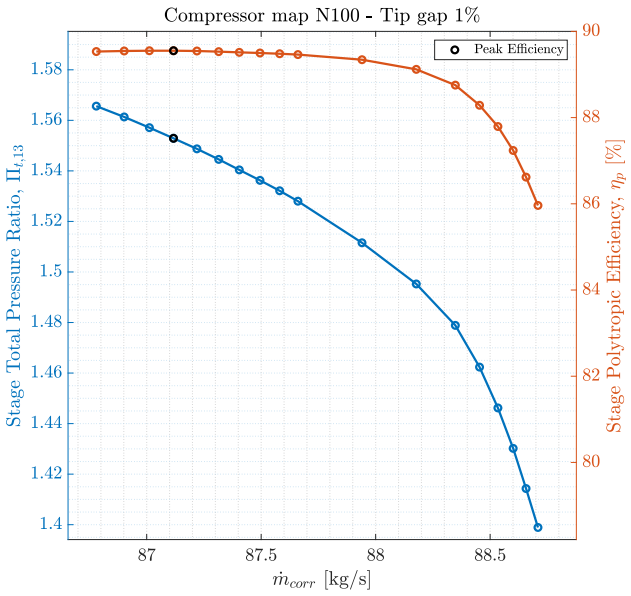

Fig. 4.1. R1S1B Compressor Map with 1% Tip Gap at nominal speed

Figure 4.1 displays the compressor map at nominal speed with a tip gap of 1% of the blade span (1.3mm). This compressor map corresponds to the one displayed in Figure 3.7 for *Mesh 03*. It is generated simulating a throttling by gradually increasing the back pressure, i.e. the static pressure at the stage outlet (stator outlet interface). The back pressure ranged from 53kPa to 63.5kPa, finding the PE point at a back pressure of 62.25kPa.

Table 4.1 summarizes the main features extracted from the compressor map:

TABLE 4.1. CHARACTERISTIC COMPRESSOR MAP OPERATING POINTS

OP	Back Pressure [kPa]	Efficiency [%]	Corrected Mass flow [kg/s]	Pressure ratio [-]
NC	53	85.96	88.71	1.399
PE	62.5	89.55	87.12	1.553
NS	63.25	89.53	86.78	1.566

4.1.2. Local flow effects - Smooth case

Before getting into the study of the impact of surface roughness on the compressor stage, it is important to look closely at the baseline behavior of the flow, removing the roughness contribution. It is essential to identify how the flow behaves in an ideal situation, ideal here meaning with all the walls featuring a smooth surface. Once the flow mechanisms are detected, the impact on the performance and characteristic variables of the compressor can be understood.

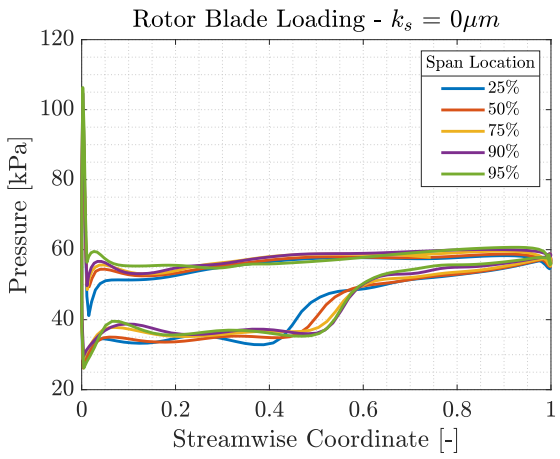

Fig. 4.2. Rotor blade loading - Smooth case

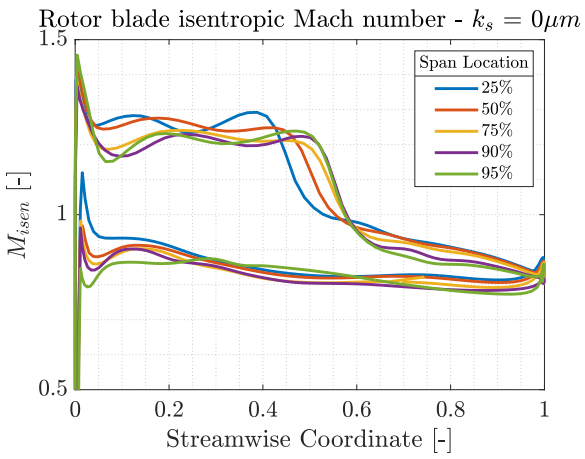

Fig. 4.3. Rotor blade isentropic Mach number - Smooth case

Streamwise charts provide information regarding the flow features along the blade at different span locations. The blade loading (pressure along the blade) and isentropic mach number distribution charts provide a clear view of the evolution of the pressure and Mach number field on the blade, providing information regarding shock waves, incidence angles, etc. Figure 4.2 and Figure 4.3 display the blade loading and isentropic Mach number corresponding to the baseline or smooth case, for a set of five different spanwise locations (25%, 50%, 75%, 90%, 95%), respectively. First of all, by looking at the sudden decrease to subsonic isentropic Mach number around the 0.5 streamwise location on Figure 4.3, the passage shock can be identified. This is linked to the rapid increase in pressure at the same location in Figure 4.2. Moreover, the displacement of the shock wave to the rear part of the blade as the span location moves closer to the shroud can be clearly detected. Another important conclusion that can be extracted from this type of graphs is the change in incidence angle. In Figure 4.2, close to the LE, at streamwise positions close to zero, the pressure amplitude between the pressure and suction surfaces provides information on how the flow angle changes from the designed configuration. A more positive or more negative flow angle will lead to a larger amplitude in the blade loading plot at the LE region.

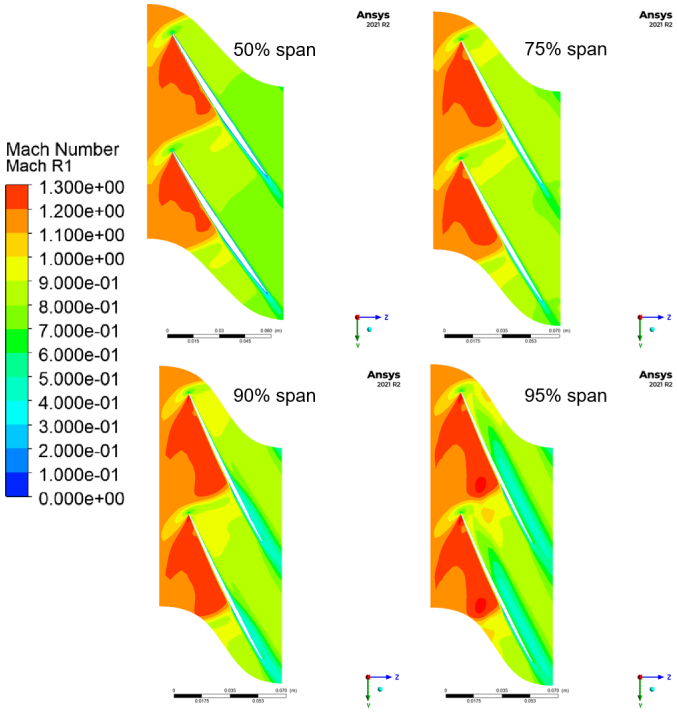

Fig. 4.4. Mach number contours - Smooth case - Rotor domain

Figure 4.4 displays the relative Mach number contours at different spans of the rotor domain. The main feature extracted from the Mach number is the presence of two shock waves. One coming from the LE, leading to a detached bow shock. The other is found at the passage and is directly related to the bow shock of the neighboring blade. This is a normal shock wave and it is one of the main flow features present in a transonic compressor rotor. After the LE bow shock, an acceleration region is found reaching Mach numbers between 1.3 and 1.4 depending on the spanwise position. This acceleration is followed by the passage normal shock causing a clear sudden deceleration of the flow in the passage, decreasing the Mach number to values between 0.9 and 0.6. As the spanwise position increases, the initial acceleration region gets larger, thus pushing the normal passage shock to move downstream. At 90 and 95span, the tip gap vortex is identified due to the lower Mach number found at the pressure surface and that extends from half the blade chord to the outlet region.

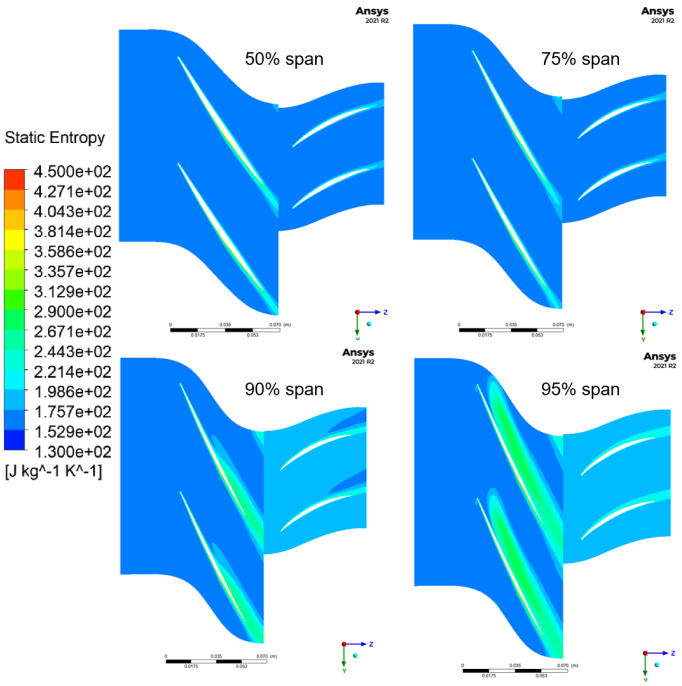

Fig. 4.5. Static entropy contours - Smooth case - Entire domain

Figure 4.5 displays information regarding the static entropy distribution at different span locations for both the rotor and stator domains. Static entropy contours allow to see a clear image of the wake and boundary layer of both blades, i.e regions with high losses. An increase of rotor wake width is noticed as the span position increases (as it moves towards the tip/shroud). At 90% span, the tip vortex can be detected, represented by a region of higher entropy generation at the pressure surface of the blade close to the TE. This vortex has an effect on the stator region due to the non optimized geometry of the stator blade to this specific configuration, where a rotor tip gap is included. At higher spanwise locations, entropy generation increases on the whole stator domain being able to identify a much broader stator wake. At 95% span these effects become much larger.

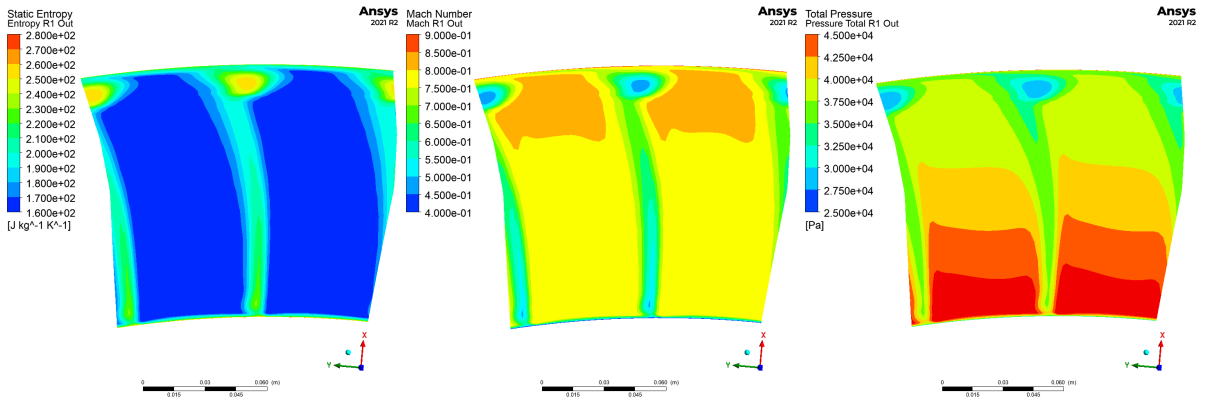

(a) Static entropy (b) Mach number (c) Total pressure

Fig. 4.6. Flow variables at rotor outlet

Radial plots (Figures 4.6 & 4.7) provide a clear view of the spanwise distribution of different flow features at a specific streamwise location. They also provide the effects of the presence of the blades in the passage, allowing to assess the variables from a different perspective, for example the wake or the vortices. The static entropy contour, similar as with the axial plane plots, gives a clear picture of the size of the blade wake, in this case having a direct assessment of its width variation along the spanwise direction. Moreover, close to the shroud, and corresponding to the tip gap region, the tip vortex can be identified with a much larger entropy generation area with circular shape. Mach number contour in this case, does not provide much extra information, however it is here presented as it will be useful in further sections to perform the comparison between the different rough cases. Total pressure contour shows a radial distribution with decreasing total pressure from the hub to the shroud, mainly due to the variation in velocity from hub to shroud. Furthermore, once again, the tip vortex is pictured by the region with the lowest total pressure, due to the lower axial velocity and high rotational momentum.

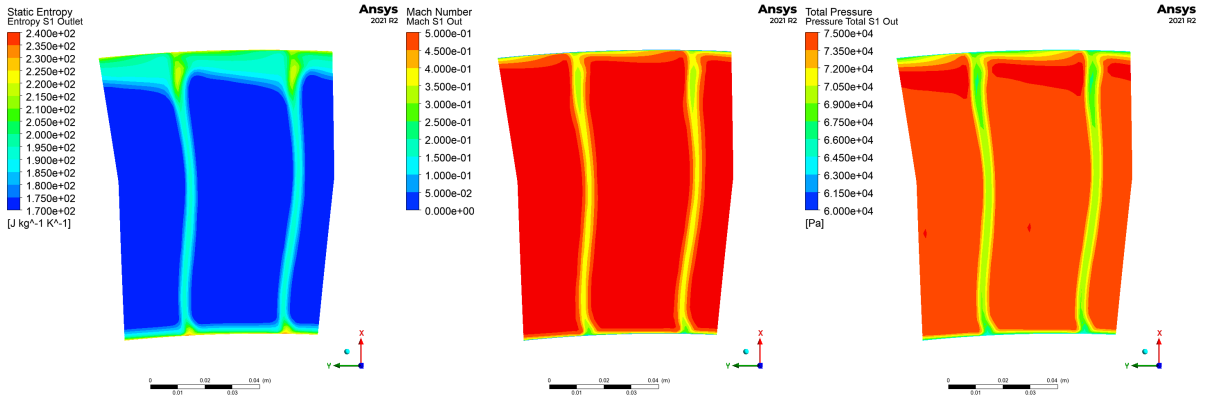

(a) Static entropy (b) Mach number (c) Total pressure

Fig. 4.7. Flow variables at stator outlet

For the stator, the clearest difference is the absence of the tip vortex and the absence of the effect of the blade rotational velocity. With this, there is a lack of radial variation of the pressure or Mach number. By looking at the static entropy plot, it can be clearly perceived the effect of the rotor tip gap on the stator, due to the larger entropy production at the tip region. Furthermore, a short region containing the horseshoe vortex can be also identified close to the hub and shroud of the machine. This effect is much larger at the shroud due to the influence of the tip gap vortex coming from the rotor domain.

4.1.3. Rough Cases

A set of rough cases was defined. The sandgrain roughness height ranges from 0 to 63μm presenting a total of 7 cases, in addition to the smooth or baseline case. k_s=0 and 0.5μm lie in the hydraulically smooth regime, while the rest of the cases (k_s=10, 25, 40, 50, 60 and 63μm)

lie in the transitionally rough regime. Table 4.2 displays a summary with the some equivalence between k_s and k_s^+, as well as identyfing their roughness regimes.

TABLE 4.2. ROUGHNESS REGIMES

k_s [μm]	k_s^+	Roughness regime
0	0	Hydraulically smooth
25	13.44	Transitionally rough
60	32.34	Transitionally rough
63	33.88	Transitionally rough

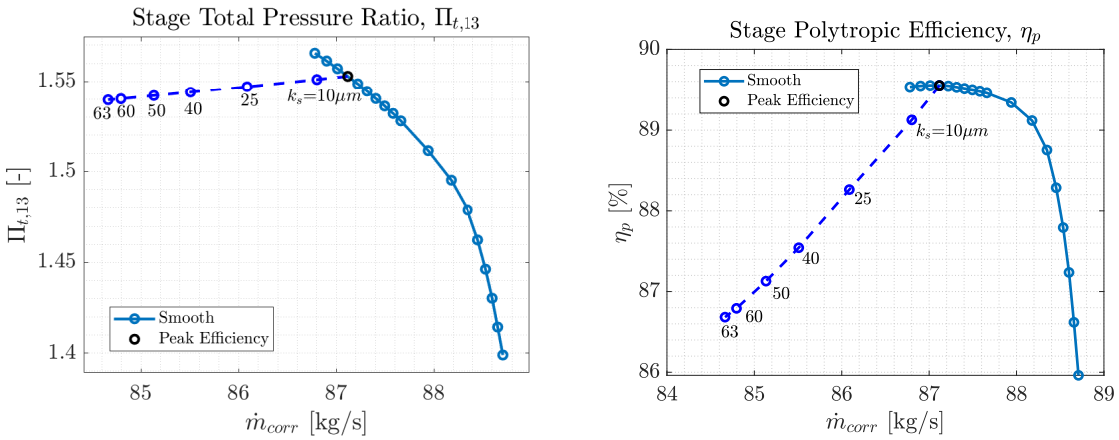

(a) Stage total pressure ratio

(b) Polytropic efficiency

Fig. 4.8. Roughness effects on compressor map variables

Figure 4.8 displays the impact of surface roughness on the compressor map variables, for the PE operating point as this is the target OP to perform the flutter analysis. Both the efficiency and pressure ratio decrease with increasing roughness height, as well as reducing the mass flow ratio across the stage. This is mainly due to the blockage effect provoked by the roughness elements as well as the increase in skin friction, as predicted and observed in other studies [2, 7, 9, 16, 17]. The relative impact on performance is much larger than the one on pressure ratio, with a maximum loss of 3 points for the roughest case studied. Moreover, The most interesting conclusion observed from these results is the existence of an upper limit in roughness. For larger roughness values than 63μm, the simulations could not converge, thus setting here the maximum value of roughness to be studied. The principal hypothesis extracted from this situation is the anticipation of blade stall due to the increase in roughness, thus provoking a change in effective area due to the blockage effect. To confirm this, the complete speedlines for each case must be computed, being able to observe the effect of roughness on the main operating points of the compressor. However, the stall hypothesis is consistent with the local flow phenomena observed, where a change on incidence angle occurs due to the increase in roughness.

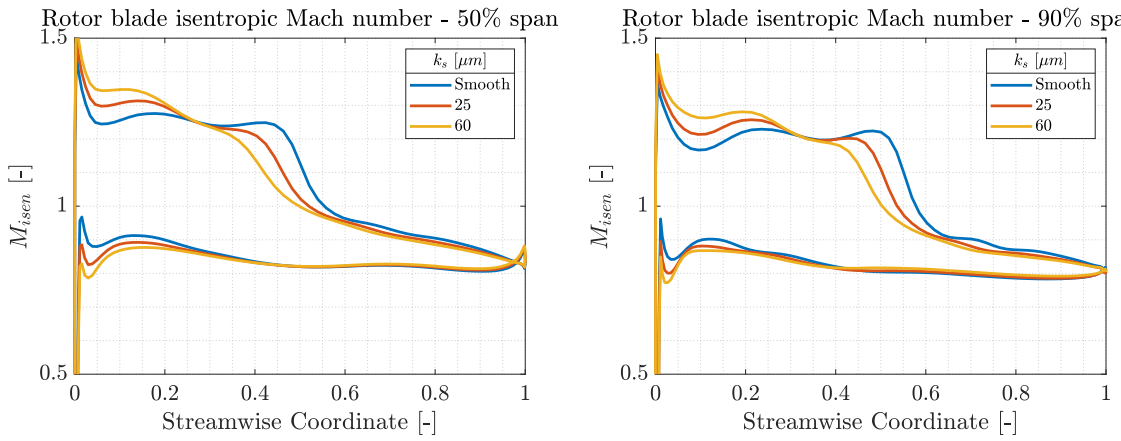

(a) 50% span (b) 90% span

Fig. 4.9. Roughness effects on rotor blade isentropic Mach number distribution

The change in incidence angle can be clearly observed in Figure 4.9, among other phenomena. In these two figures, the rotor blade isentropic Mach number distribution is plotted for two different span locations, comparing three rough cases: smooth, 25μm (medium), and 60μm (close to limit). At both locations, an increase in incidence angle can be detected by the isentropic Mach number difference, ΔM_{isen}, found between the pressure and suction surface close to the leading edge. A higher ΔM_{isen} at this location means an increase in incidence angle. In addition, between the streamwise locations of 0.4 and 0.6, the passage shock at the suction surface is captured, manifested as a sudden decrease in Mach number to subsonic values. Roughness clearly affects both the location and the strength of the shock. As roughness increases, the shock is pushed towards the LE, and its strength is reduced, represented by a more gradual decrease in M_{isen}. These effects are observed at both span locations, suggesting that the uniform roughness distribution implemented presents the same trends no matter the spanwise location on the blade.

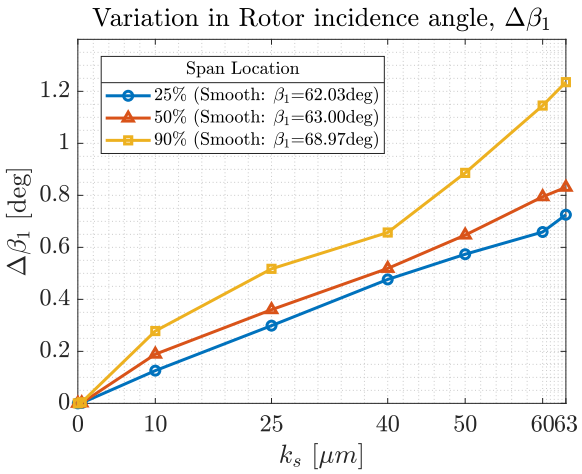

Fig. 4.10. Variation in rotor relative inlet flow angle, $\Delta\beta_1$ Vs. Sandgrain roughness height, k_s

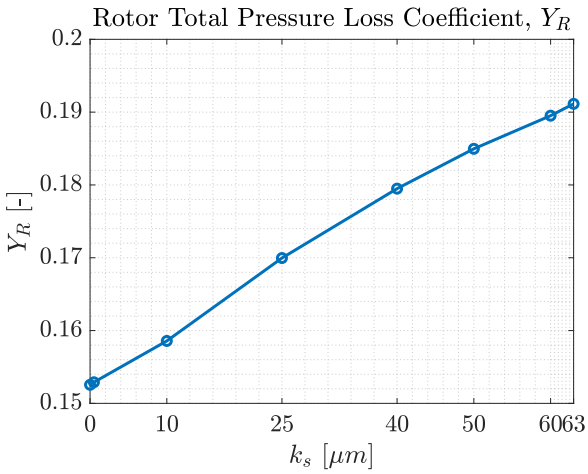

Fig. 4.11. Rotor total pressure loss coefficient, Y_R, Vs. Sandgrain roughness height, k_s

Figure 4.10 and Figure 4.11 allows to evaluate quantitatively the change in incidence angle

due to roughness and the pressure loss across the stage as defined in Equation 4.1, respectively.

$$Y_R = \frac{P_{01,rel} - P_{02,rel}}{P_{01,rel} - P_1}, \tag{4.1}$$

where $P_{01,rel}$ and $P_{02,rel}$ refer to the rotor relative total pressure at rotor inlet and outlet, respectively, and P_1 to the static pressure at the inlet of the rotor domain.

First, $k_s = 0.5\mu$m does not produce any substantial change, as expected. Incidence angle and pressure loss remain below a 1% difference with respect to the smooth case, as predicted in similar studies on the topic [2, 9]. A maximum change in incidence of almost 1 degree is observed at 50% span location. A one-degree change in incidence angle can be considered as a high variation for a transonic compressor, leading to considerable differences in the local flow phenomena and overall performance. This is consistent with the presented results on the compressor map and pressure loss across the stage. The latter is also affected by the implementation of roughness on the blade, causing an increase in total pressure loss throughout the rotor blade row.

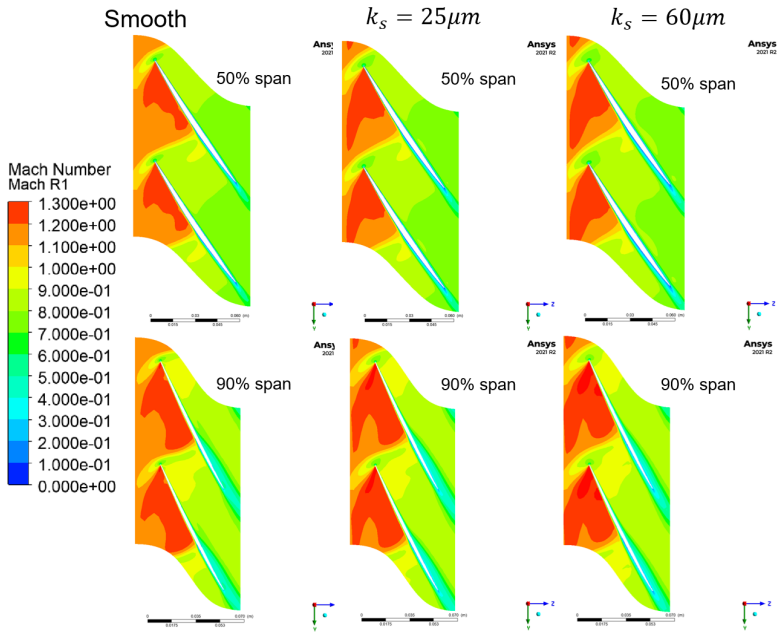

Fig. 4.12. Mach number contours - $k_s = 0, 25, 60\mu$m - Rotor Domain

Mach number contours, displayed in Figure 4.12, provide a direct comparison between rough cases. The most clear effect is the shorter and faster acceleration of the flow before the passage shock impingement. The change in incidence angle causes the flow to accelerate faster on the suction surface, anticipating the development of the shock. Moreover, the width of the wake is also increased with roughness. Skin friction becomes higher, and so the size of the boundary layer. At higher spanwise locations, the tip gap vortex can be observed. This is also affected by surface roughness, increasing the strength and size of the vortex.

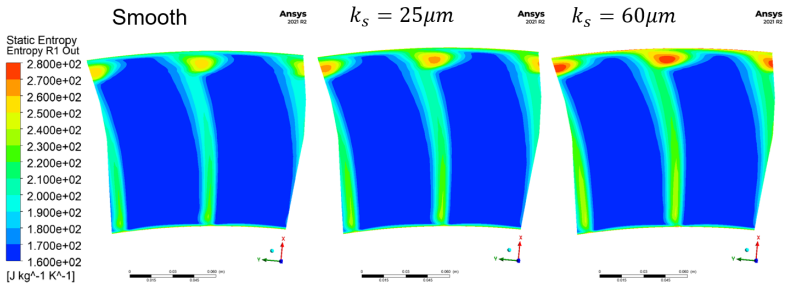

Fig. 4.13. Static entropy contours - k_s = 0, 25, 60μm - Rotor Domain

Tip gap vortex effects are better capture by looking at the static entropy contours at the rotor outlet interface in Figure 4.13. Entropy generation gets considerably larger as roughness height increases. The size and strength of the tip gap vortex increase gradually. In addition, this plot also allows to compare directly the size of the wake, identifying a much wider wake for larger values of k_s.

$\mathbf{k_s}$ [μm]	0	25	60
$\eta_{p,rotor}$ [%]	92.55	91.64	90.66
$\dot{m}$ [kg/s]	41.83	41.34	40.72
Blade Loading [N]	1347.27	1358.64	1365.31
$\Pi_{tt,rotor}$ [-]	1.568	1.563	1.559
Y_{rotor} [-]	0.15255	0.16996	0.18950

TABLE 4.3. TABULATED STAGE CHARACTERISTIC VARIABLES FOR k_s = 0, 25, 60 μm

Table 4.3 provides a summary of the main variables across the stage for three values of k_s. Rotor blade loading gets notably higher as the operating conditions are changing with increasing roughness, suggesting a more loaded compressor stage, therefore directly modifying one of the main design variables of the machine.

4.2. Transient: Flutter Analysis

This section is intended to show the final output of the study. First of all, the results regarding the aerodynamic damping are presented. Secondly, the different cases presented in the aerodynamic damping plots are compared and the different trends identified in order to have a clear view of the results obtained.

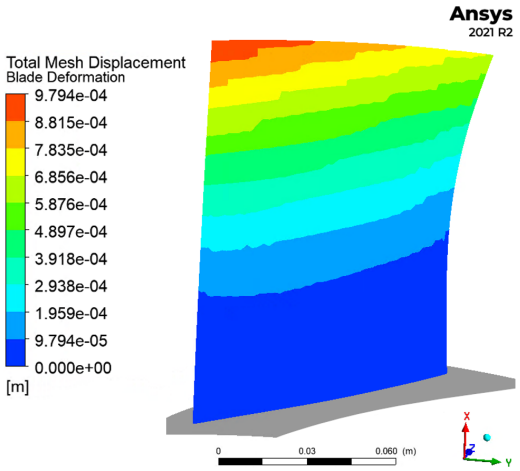

Fig. 4.14. Total mesh displacement for 1B mode

The total mesh displacement corresponding to the 1st Bending Mode is represented in Figure 4.14. Maximum blade displacement was scaled so it is 1% of the blade true chord at mid span (0.98mm).

4.2.1. Aerodynamic damping S-curves

Aerodynamic damping S-curve allows to evaluate the aeroelastic stability for the whole domain of nodal diameters. The process to get the complete set of nodal diameters for a set of k_s values is computationally demanding, as it requires solve for the aerodynamic damping for each case separately. So, for the purpose of this project, a reduced set of seven nodal diameters was computed, presenting ND0, ND(±3), and ND(±15). In this context, "+" refers to FTW, and "-" means BTW. Moreover, the original k_s set used for the steady-state cases was also reduced from seven values to only three. It features a smooth case, $k_s = 25\mu$m, typical value found in real applications after 20,000 cycles [7], and $k_s = 60\mu$m, serving as a reference of a roughness limit value, as it was found out in the steady-state analysis.

The first step concerns the comparison of the smooth case with the reference case from Lejon *et al.* [60]. The idea was to check the orders of magnitude as well as the trends observed. Figure 4.15 presents the results comparing the reference case without tip gap and the computed S-curve for the present study taking the tip clearance effect into account.

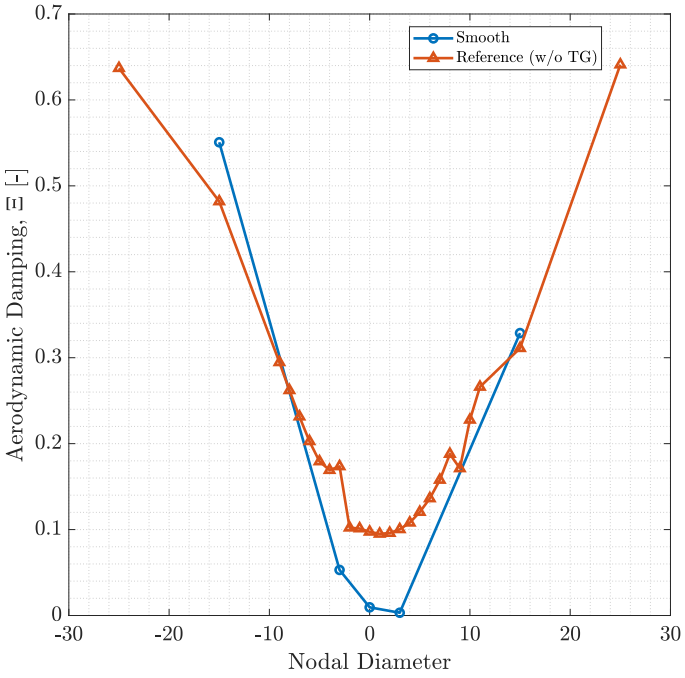

Fig. 4.15. Aerodynamic damping curve - Comparison with reference results [60]

The definition of aerodynamic damping for this purpose differs from the one presented in Equation 2.26. The data available from the article, and thus the results on Figure 4.15, were computed applying the following definition [60]:

$$\Xi = \frac{W_{\text{cycle}}}{\pi L (u_{\text{max}})^2 p_{\text{ref}}} \tag{4.2}$$

This equation presents a different way of normalizing the value of the work-per-cycle, using a reference pressure, $p_{\text{ref}} = p_0 - p_1$ (where p_0 is the average relative total pressure and p_1 is the average static inlet pressure), blade span, L, and the maximum deflection of the blade, u_{max}. First thing that has to be mentioned when looking at Figure 4.15 is the presence of the same order of magnitude in the values, ranging from values close to zero for the least stable NDs ($|\text{ND}| \leq 3$), up to values of 0.7 for the most stable NDs ($|\text{ND}| > 3$). Furthermore, the trends are also the same. Both aerodynamic damping curves present an absolute minimum at ND≈3. The effect of the tip clearance is manifested in a substantial decrease in stability for the least stable nodal diameters.

In order to carry out the final stability analysis, the critical aerodynamic damping definition from Equation 2.26 is recovered. The final output after computing the proposed nodal diameters for the three sandgrain roughness heights is presented in Figure 4.16:

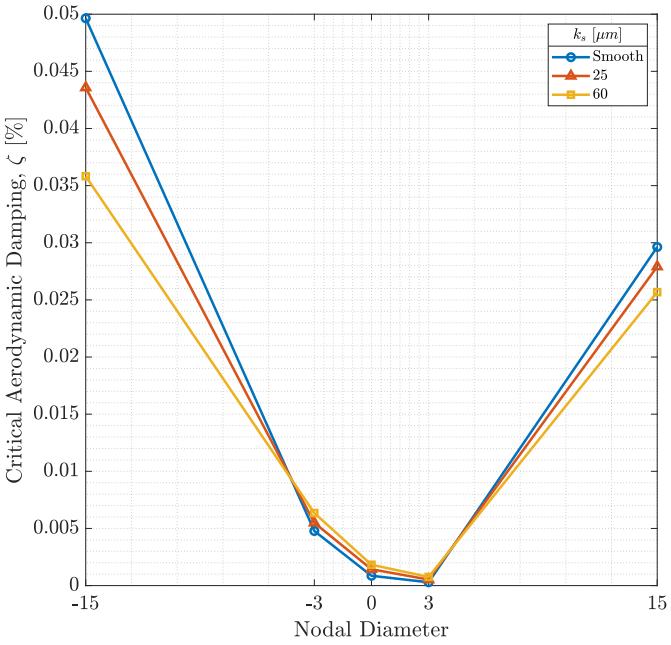

Fig. 4.16. Aerodynamic damping curve - Roughness impact

The values are one order of magnitude less than those of Figure 4.15. However, the focus here is on trends due to the effect of roughness on the aeroelastic stability of the system, as these results are not going to be compared with experimental data. First of all, changes in roughness do not modify the shape of the S-curve. The three surfaces show the same behavior, featuring the absolute minimum for ND3. Moreover, roughness has a very different impact for the different nodal diameters. It is clear that for the least stable nodes, $-3 \leq \text{ND} \leq +3$, roughness has a positive impact in the aerodynamic damping, increasing slightly the stability of this nodal diameters, pushing them away from the critical stability limit, at $\zeta = 0$. The opposite happens when looking at more stable nodal diameters, $|\text{ND}| > 3$, where increasing roughness intensity clearly decreases the value of the aerodynamic damping, deteriorating the stability of the system. Despite this fact, the effect of surface roughness in these nodal diameters does not threaten the risk of flutter inception, as the value of the aerodynamic damping still remains far from the critical limit, staying as the maximum values for each roughness height. The trends here presented may be a direct consequence of the change in operating point due to surface roughness. As a result of the blockage effect introduced by the surface roughness implementation in CFX, incidence angle changes, and thus the operating conditions are affected by this. Therefore, passage shock strength and location, together with changes in the unsteady pressure distribution could be the reason to the results presented in Figure 4.16. The following section is addressed to look at the individual cases and find disparities for the results on the aerodynamic damping.

4.2.2. Local flow phenomena

In order to understand the mechanisms leading to the aerodynamic damping results previously presented, the analysis is going to be focused on the evaluation of the wall work density, and unsteady pressure phase and amplitude distributions. In addition, the steady-state results also serve as an useful mean to perform the analysis. The research is divided in three parts: two of them performing a roughness comparison for two different nodal diameters, ND0 and ND(-15), and a nodal diameter comparison fixing the value of the sandgrain roughness at 25μm.

Wall work density, in Figure 4.18a, is a direct indicator of the damping of the blade. This variable represents the work (per unit area) performed by the blade against the fluid due to the motion, and this graph displays the distribution at constant spanwise locations, for both the suction and pressure surfaces. The sign of the WWD corresponding to each blade surface is recovered from Equation 2.27, as it depends on the direction of the movement of the blade for a instant. The phase instant displayed for each WWD plot corresponds to a velocity vector pointing towards the pressure surface, thus recovering always positive values for the Pressure Surface (PS), and negative values for the Suction Surface (SS). Positive values are related to aeroelastic stability, meaning that the blade is aerodynamically damped by the flow. The figure on the right, Figure 4.18b, shows the amplitude and phase of the unsteady pressure on the blade. The unsteady pressure is computed as the sum of all the Fourier coefficients contribution. To compute the amplitude, A, and phase, ϕ, the following formulas were applied, where A_0 refers to the steady-state value, and A_1 and B_1 to the first real and imaginary Fourier coefficients, respectively:

$$A = \sqrt{A_1^2 + B_1^2} \tag{4.3}$$

$$\phi = \arctan \frac{B_1}{A_1} \tag{4.4}$$

$$F(t) = A_0 + A_1 \cos(\omega t) + B_1 \sin(\omega t) = A_0 + A \cos(\omega t + \phi) \tag{4.5}$$

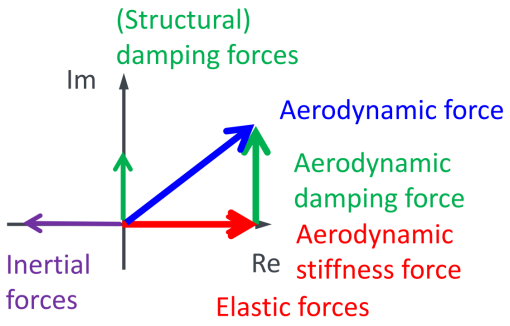

Fig. 4.17. Aerodynamic forces diagram [69]

Figure 4.17 displays a scheme with the forces involved in the system. The amplitude, A, represents the module of the aerodynamic force vector, while the phase, ϕ, gives the angle

between the real and imaginary forces. Any positive angle, higher than zero and lower than 180^o, leads to a positive aerodynamic damping. Any other value ($-180 \leq \phi \leq 0$) implies zero or negative aerodynamic damping, and therefore contributing to the risk flutter onset.

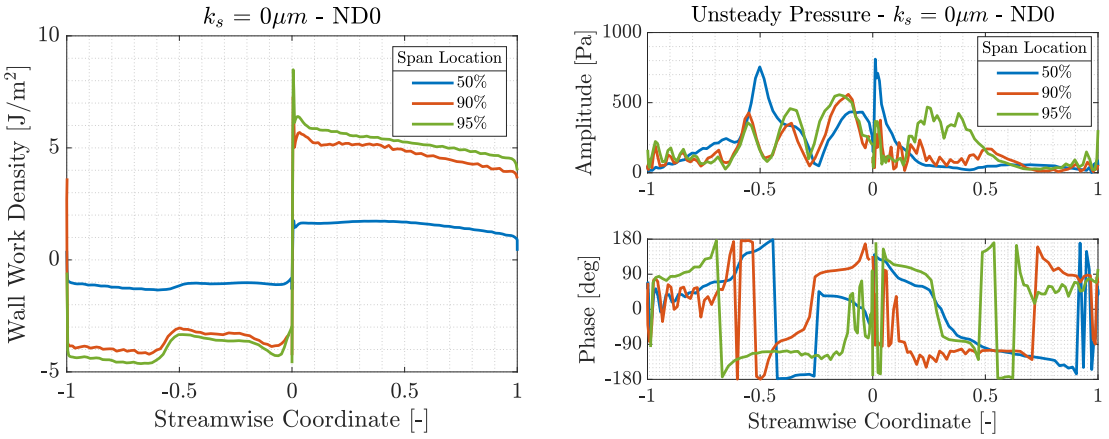

(a) Wall work density

(b) Unsteady pressure: Amplitude & phase

Fig. 4.18. k_s= 0μm - ND0

Wall work density presents a negative value on the suction surface, while it is positive on the pressure surface. Moreover, the absolute value of the WWD clearly increases as the spanwise location moves closer to the tip. This shows the matching between this variable and the mode shape, which also features higher displacements at the blade tip, as can be seen from Figure 4.14. The shape of the WWD distribution is directly related to the mode shape as it features the projection of the unsteady pressure over the blade velocity vector. Unstable pressure amplitude and phase distributions lead to slight changes in the WWD, having a great influence on the final stability of the system. High amplitudes and positive phase values lead to an increase or a more positive WWD distribution. The opposite happens if the amplitude is kept high, but the unsteady pressure phase moves to the negative side. Areas with low amplitudes exhibit a decrease in WWD variation, regardless of the phase value, maintaining the trends in those regions. This effects can be seen on Figure 4.18, where close to the LE, the sign of the WWD is reversed because the vector of displacement is collinear with the normal area vector but with different directions. At this point, the amplitude of the unsteady pressure has a peak with a positive phasing.

After an overview of the variables to be used for the analysis is given, the actual comparison is presented in the following pages. The analysis is divided into three parts, two of them comparing the results of two different nodal diameters, ND0 and ND(-15), and another to analyze the effect of the nodal diameter by fixing the roughness value at $k_s = 25\mu$m.

Nodal diameter comparison. Fixed k_s = 25μm.

When comparing different NDs, it can be seen from the aerodynamic damping curve (Figure 4.16) that the stability decreases as the ND gets closer to zero.

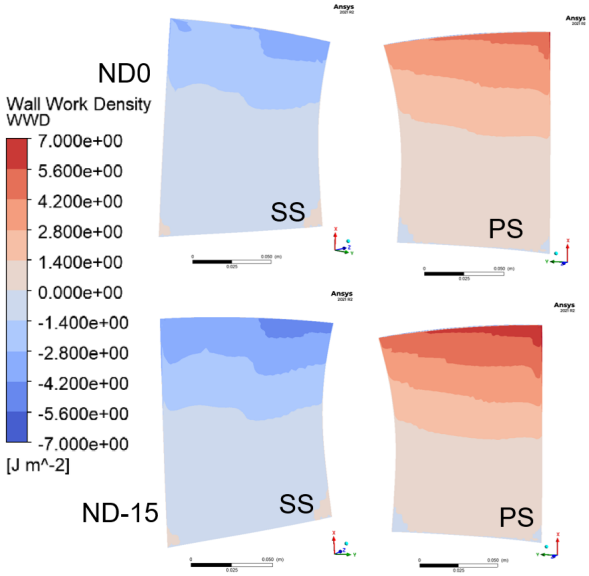

Fig. 4.19. Wall work density contour for k_s= 25μm. Nodal diameter comparison: ND0 (top) Vs. ND(-15) (bottom)

Figure 4.19 shows the WWD contour at a fixed roughness value of k_s= 25μm, for ND0 and ND(-15). For both nodal diameters, the WWD displays the same shape, with the maximum values located at the tip of the blade. From these plots, it can be observed a higher value of the WWD for the ND(-15). However, it is difficult to quantify and identify the reasons affecting the different values for the aerodynamic damping just by looking at these contour plots. There are no clear differences on the suction and pressure surface that may result in an increase or decrease on aerodynamic damping. For this reason, it is required to look at disparities on the unsteady pressure field that may be linked to a change in the aeroelastic stability.

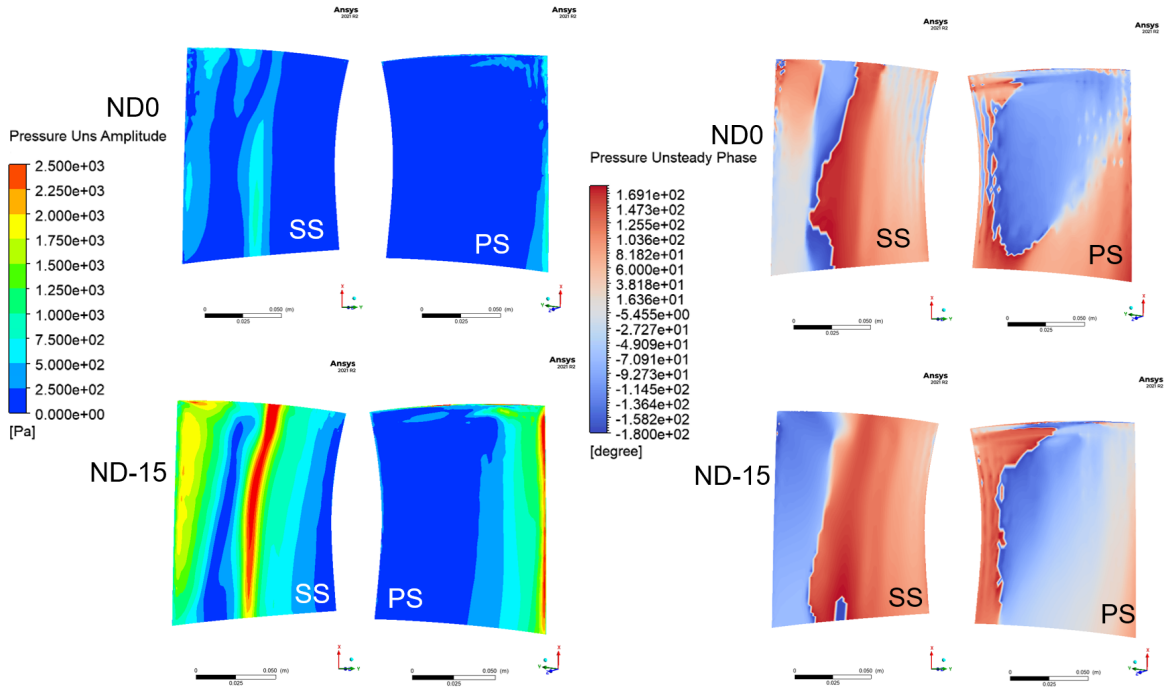

(a) Unsteady pressure amplitude: ND0 (top) Vs. ND(-15) (bottom)

(b) Unsteady pressure phase: ND0 (top) Vs. ND(-15) (bottom)

Fig. 4.20. Unsteady pressure amplitude and phase for k_s= 25μm. Nodal diameter comparison.

Figure 4.20 displays the contour plots for the unsteady amplitude and phase on the whole surface of the blade. This allows to have a qualitative idea of the main differences between cases. Figure 4.20a shows a clear difference in the maximum amplitude between ND0, featuring the lowest aeroelastic stability, and ND(-15), showing the highest aerodynamic damping. The maximum amplitude appears on a hub-to-tip line around 45% of chord on the SS, clearly corresponding to the location of the passage shock. As already predicted in the steady-state analysis, the main physical contribution affecting the aeroelastic stability is the location and intensity of the passage shock. However, this is not the only factor influencing the aerodynamic damping. When comparing different NDs, the phasing between adjacent blades, i.e. the IBPA, also controls the stability by means of the changes in relative position of one blade with the neighboring ones. In terms of phasing contours, in Figure 4.20b, it is a bit more complex to check for possible differences to justify the changes in damping. Nevertheless, clear differences can be observed simply by examining the phasing distribution, with ND(-15) showcasing a more uniform pattern on the suction and pressure surfaces of the blade. In Figure 4.20b, it is difficult to check where the phase features values close to +90deg or -90deg. Identifying regions with these phasing values is crucial as they will define which areas might have a positive or negative contribution to the aerodynamic damping, according to Figure 4.17.

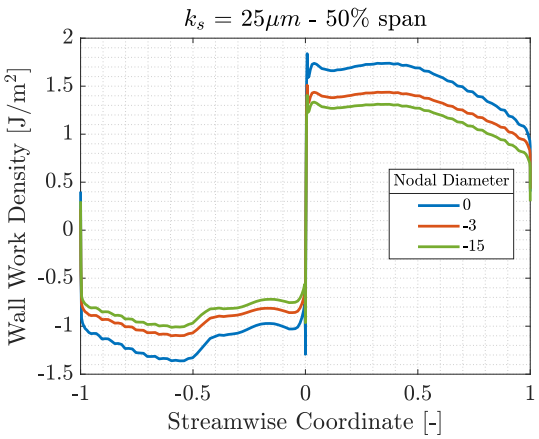

(a) Wall work density

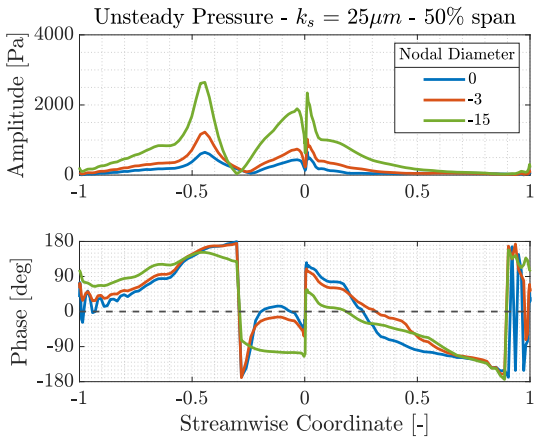

(b) Unsteady pressure: Amplitude & phase

Fig. 4.21. k_s= 25μm at 50% span. Nodal diameter comparison

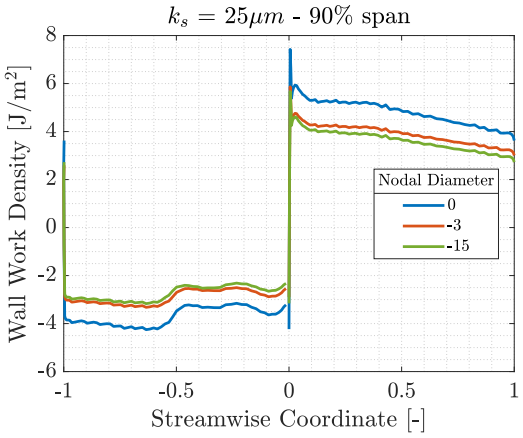

(a) Wall work density

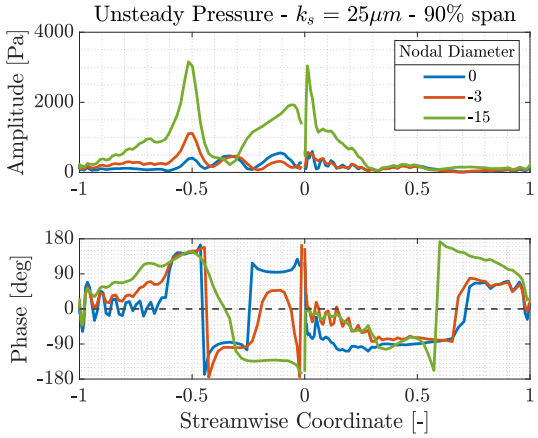

(b) Unsteady pressure: Amplitude & phase

Fig. 4.22. k_s= 25μm at 90% span. Nodal diameter comparison

To perform a quantitative analysis of the unsteady pressure and wall work density, plots at 50% and 90% span were generated. Just by looking at the streamwise plots of the WWD for different NDs in Figures 4.21a and 4.22a, it can be seen an increase in WWD difference between the SS and PS as the ND moves away from zero. The distributions here presented are plotted for one specific time instant. In this case, the time instant corresponds to the moment of maximum WWD in order to have a better comparison between cases. As the results are always extracted from the blade leading the motion, all the cases here displayed are in phase and so the shapes and magnitude differences are preserved, no matter the time instant chosen. WWD figures only provide with a quantitative idea of the differences between cases at very specific locations. In order to have a more accurate idea of how the WWD is affecting the stability, this should be integrated over the blade, thus losing information in terms of its distribution on the blade. The fact that the WWD exhibits notable differences between cases, allows to understand the changes in aerodynamic damping values.

Figures 4.21b and 4.22b allow to have a better understanding of the differences shown in the WWD. As the WWD is nothing else than the projection of the unsteady pressure on the mode shape, analysing the unsteady pressure amplitude and phase helps to isolate the phenomena going on for each case. Two amplitude peaks can be identified, one on the SS corresponding with the position of the passage shock, and another located at the LE of the blade. The passage shock amplitude peak appears to be in-phase (≈120deg), clearly damping the motion. The amplitude of the peak increases for ND(-3) and ND(-15). This appears to be one of the main reasons for the higher WWD on the SS for these two cases. Moreover, on the PS, something similar happens, with a higher LE amplitude peak for the ND(-15) case, while it remains in-phase just at this streamwise location. A change in phase shift from negative to positive values appears at the rear part of the PS, however the amplitude is very low and the possible effect on WWD is almost negligible.

Roughness comparison. Fixed ND0.

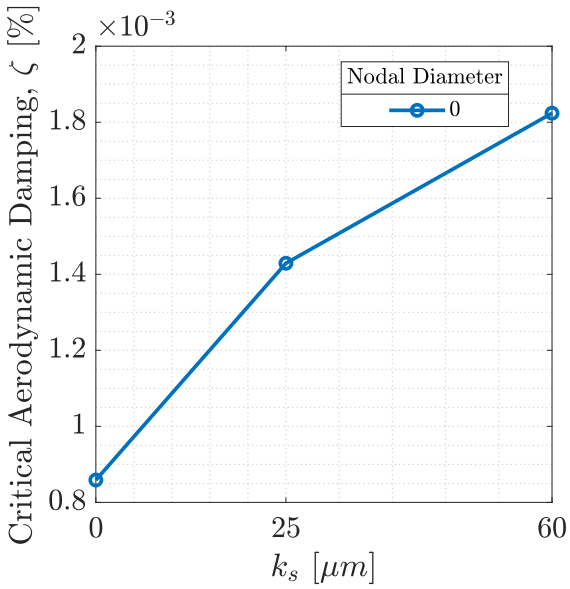

Fig. 4.23. Aerodynamic damping curve Vs. Sandgrain roughness height, k_s. Fixed ND0

From Figure 4.16, two main trends can be identified depending on the ND. When fixing the ND to zero, the impact that roughness has on the aeroelastic stability is slightly positive, featuring a little increase of the aerodynamic damping coefficient. Figure 4.23 isolates the results for ND0, being able to identify an increase of around 100% between the smooth and the most rough case. Despite this huge increase, the aerodynamic damping for this ND remains fairly low when compared to the values computed for the whole ND domain.

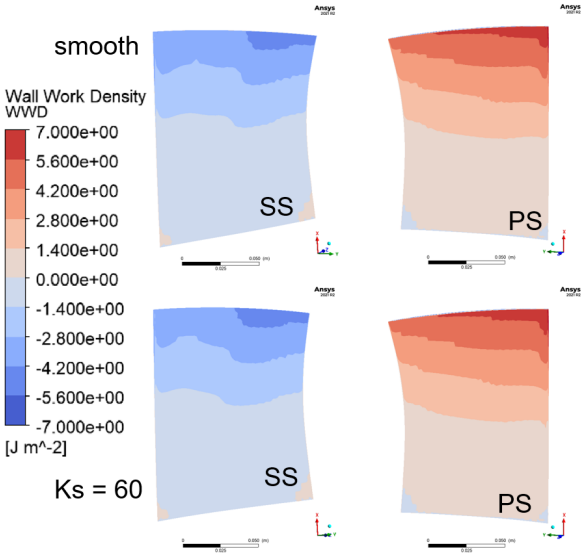

Fig. 4.24. Wall work density contour for ND=0. Roughness comparison:
k_s= 0μm (top) Vs. k_s= 60μm (bottom)

Wall work density contours in Figure 4.24 show very small differences for the different rough surfaces. Even though the aerodynamic damping value doubles for the maximum roughness case, the value is still very low compared to the others encountered in aerodynamic damping curve (Figure 4.16), and therefore the absolute difference with the damping for the smooth case remain also quite low. This can be checked when looking at the WWD contours, where the trends observed does not present remarkable differences.

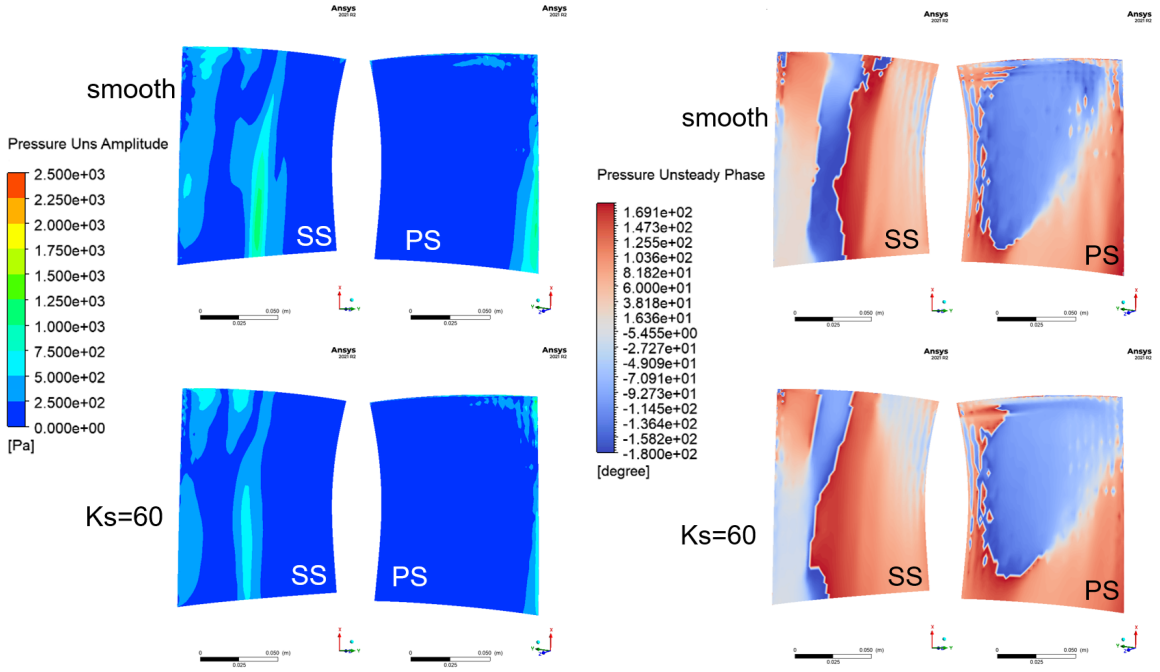

(a) Unsteady pressure amplitude: k_s= 0μm (top) Vs. k_s= 60μm (bottom)

(b) Unsteady pressure phase: k_s= 0μm (top) Vs. k_s= 60μm (bottom)

Fig. 4.25. Unsteady pressure amplitude and phase for ND=0. Roughness comparison.

First, by performing a qualitative comparison using Figure 4.25, clear differences in the unsteady pressure amplitude and phase distributions on the blade with different roughness levels can be seen. Regarding the amplitude (Figure 4.25a), principal differences appear on the SS, mainly on the area corresponding to the location of the passage shock and the acceleration region before it. Larger values of the amplitude can be seen for the smooth case. This can be linked to the lower strength of the shock as roughness increases, as demonstrated previously in Figure 4.9. The region before the shock also features magnitude and distribution differences mainly due to the change in incidence provoked by the change in roughness intensity. Phase distribution also features some disparities between cases, specifically close to the mid-span locations on the SS of the blade.

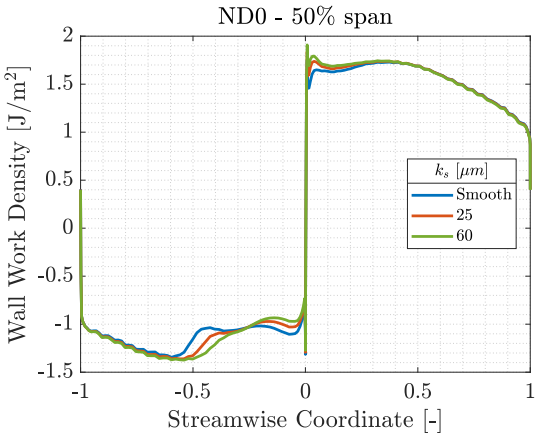

(a) Wall work density

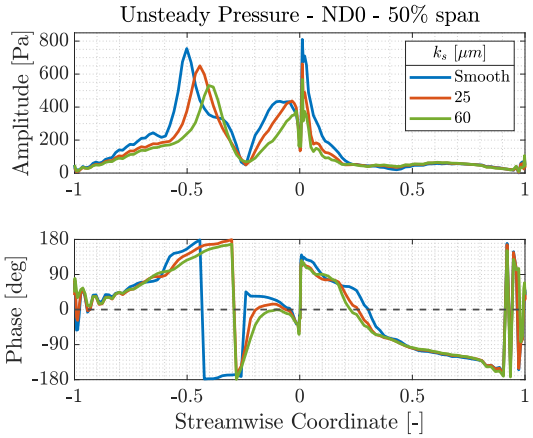

(b) Unsteady pressure: Amplitude & phase

Fig. 4.26. ND=0 at 50% span. Roughness comparison

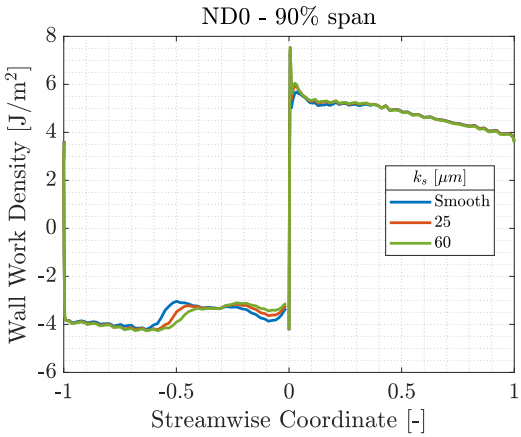

(a) Wall work density

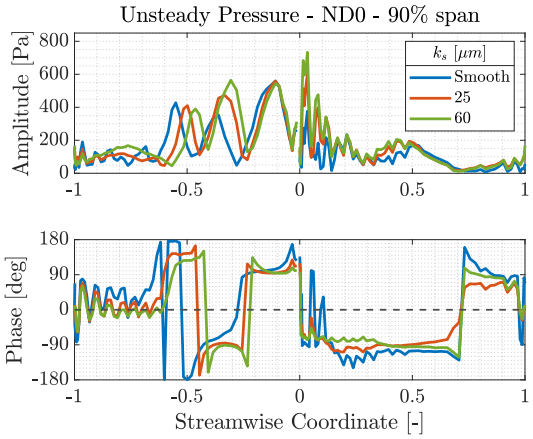

(b) Unsteady pressure: Amplitude & phase

Fig. 4.27. ND=0 at 90% span. Roughness comparison

WWD (Figures 4.26a & 4.27a) features very similar magnitude and distributions for the three roughness levels. In accordance with the unsteady pressure contours, main differences appear on the values of the SS, close to the LE and before the passage shock. Due to the change in incidence, WWD suffers a small increase on the region close to the LE at both the SS and PS. Moreover, it can be perceived how the change in the placement and strength of the shock, also changes the trends at this location, causing a small decrease in WWD. These effects can be checked at both 50% and 90% span, being the latter the one experiencing higher variations.

The variations seen in WWD can be understood by checking the unsteady pressure distribution. At both 50% (Figure 4.26b) and 90% (Figure 4.27b) span, the change in location of the passage shock on the SS can be identified around 50% of the streamwise coordinate. The difference in amplitude corresponds to the change in intensity of the shock as k_s increases. The phase at this location features a change in sign going from the negative or unstable region to

positive values, contributing positively to the stability of the system. The unsteady pressure amplitude at 90% span features more fluctuations possibly due to the instabilities arising from the tip gap region, which features a small increase in intensity due to the increase in roughness. The phase at this streamwise location is kept at -90deg, concluding that flow phenomena close to the tip presents a negative contribution to the aeroelastic stability of the system. On the PS, there are no significant variations on the amplitude or phase due to the effect of roughness.

Roughness comparison. Fixed ND(-15).

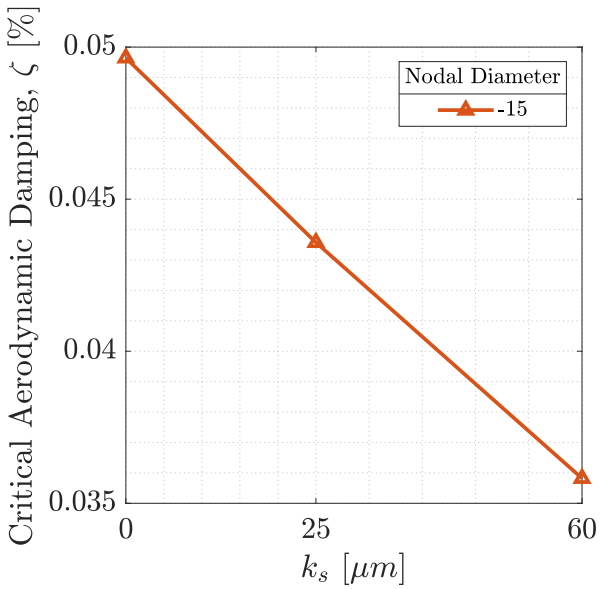

Fig. 4.28. Aerodynamic damping Vs. Sandgrain roughness height, k_s. Fixed ND(-15)

The opposite trend than the one found for ND0 is predicted for the most stable mode, corresponding to the ND(-15). In this case, a substantial decrease on the value of the aerodynamic damping is computed for increasing values of k_s. Figure 4.28 shows the corresponding decrease in damping for this mode. About a 22% of relative reduction in aerodynamic damping is encountered for the maximum roughness case when compared to the smooth one.

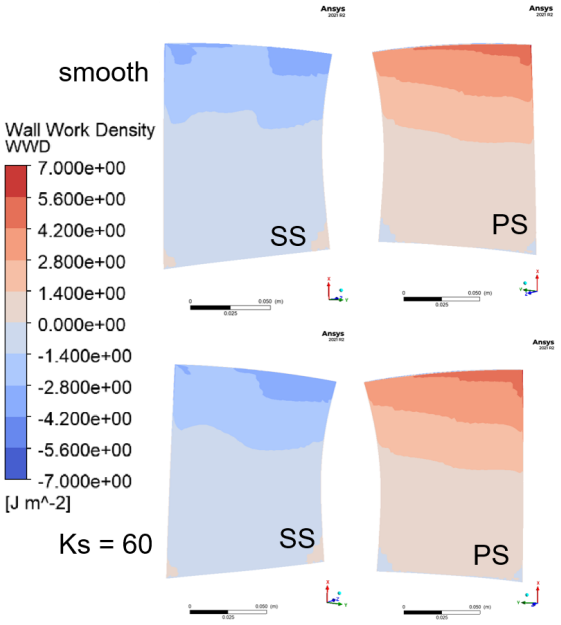

Fig. 4.29. Wall work density contour for ND=-15. Roughness comparison: k_s= 0μm (top) Vs. k_s= 60μm (bottom)

Figure 4.29 presents the WWD contours comparing the smooth (k_s= 0μm) and the maximum roughness (k_s= 60μm) cases for ND(-15). In this case, some differences can be observed by looking at the WWD distribution on the blade. First, on the PS, a slightly higher WWD region can be seen close to the leading edge for the case of maximum roughness. On the suction surface, clear differences can be noted also at the tip close to the leading edge. A localized region with lower values can be seen for the smooth case. This region is much smaller for the case of k_s= 60μm. The area corresponding to the location of the passage shock wave also displays noticeable disparities between the two cases. For the smooth case it can be seen a sharp decrease in WWD at span locations larger than 50%. On the other hand, for the maximum roughness case, it can be seen that this sudden decrease is more gradual and it is located at positions closer to the LE.

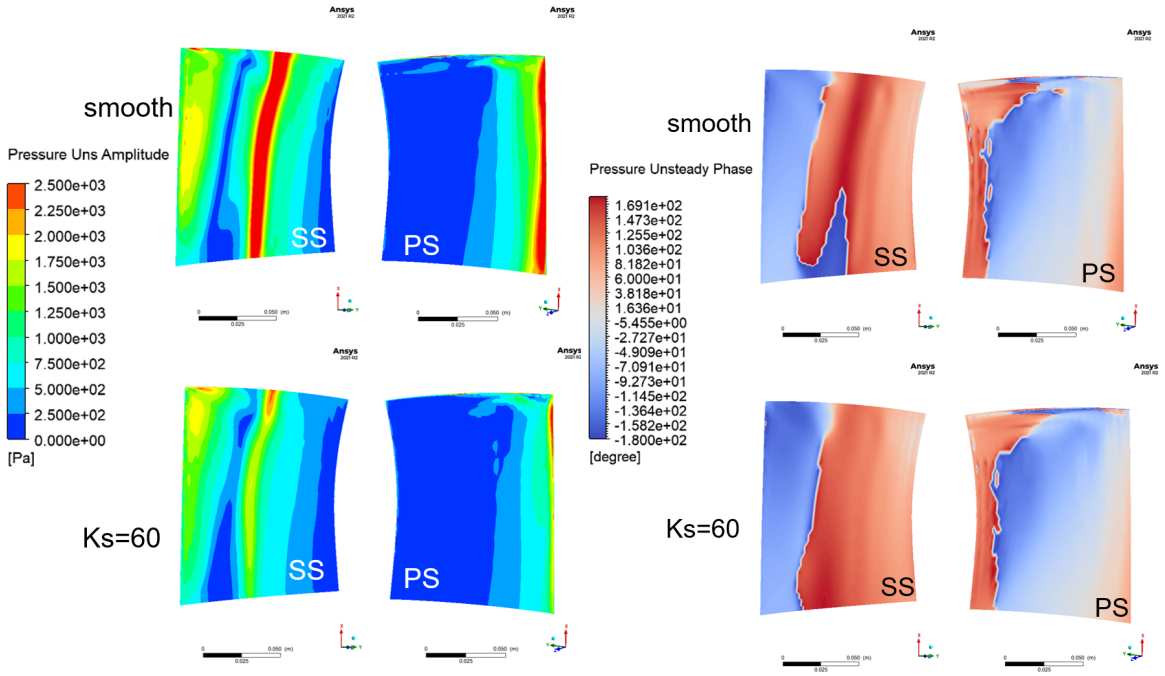

(a) Unsteady pressure amplitude: k_s= 0μm (top) Vs. k_s= 60μm (bottom)

(b) Unsteady pressure phase: k_s= 0μm (top) Vs. k_s= 60μm (bottom)

Fig. 4.30. Unsteady pressure amplitude and phase for ND=-15. Roughness comparison.

Taking a look at the unsteady pressure amplitude and phase contours, again the main differences arise at the LE and at the location of the passage shock. When compared to the previous case, with ND0, higher values for the amplitude can be clearly observed in Figure 4.30a. While the maximum amplitude in ND0 is found to be around 1000Pa, for ND(-15) the maximum amplitude goes almost up to 4000Pa. The phase distribution also appears to have big differences, especially on the suction surface, where a larger in-phase area is encountered, compared to the ND0 case in Figure 4.30b.

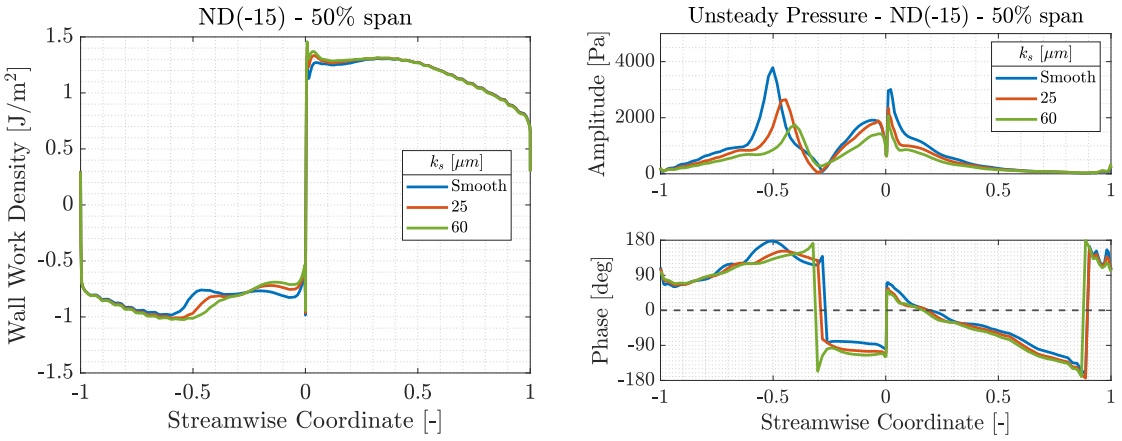

(a) Wall work density

(b) Unsteady pressure: Amplitude & phase

Fig. 4.31. ND=-15 at 50% span. Roughness comparison

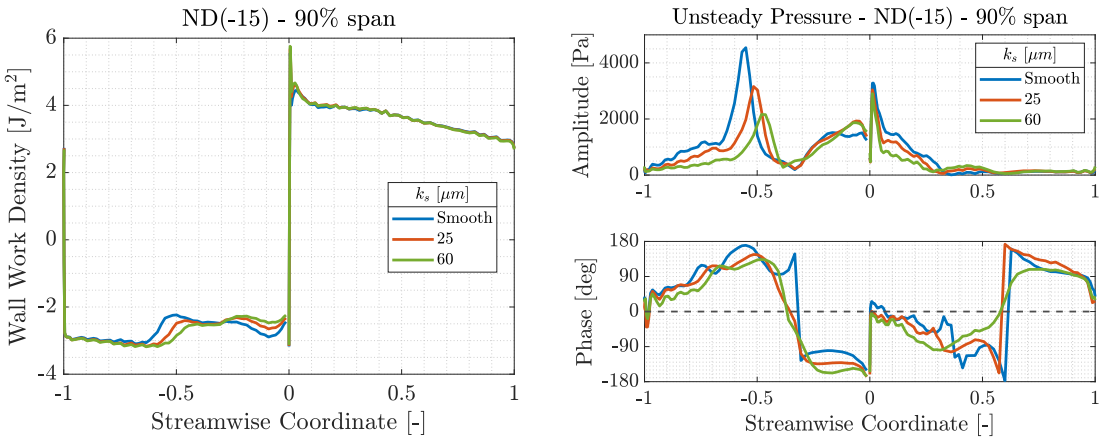

(a) Wall work density

(b) Unsteady pressure: Amplitude & phase

Fig. 4.32. ND=-15 at 90% span. Roughness comparison

Similarly as in the ND0, the WWD distribution does not present large differences between cases. Again, the values on the PS are mostly the same, except for the LE region, where the WWD features an increase with increasing roughness. In this case, it is complex to find a justification for the trends in aerodynamic damping just by looking at the WWD distribution. Unsteady pressure amplitude and phase plots present more notable differences that may be linked to the damping results. In this case, unsteady pressure amplitude presents much higher values while staying mostly in phase at the amplitude peaks, for both 50% and 90% spanwise locations. Moreover, the smooth case exhibits a high impact on the strength of the passage shock, displaying amplitude differences of more than 1000Pa. This combined with the phase, which is kept positive for most of the SS, might result in a higher aeroelastic stability globally. On the PS, the differences are smaller, however, a slight decrease in amplitude can be seen at the LE as roughness increases.

5. CONCLUSIONS & FUTURE WORK

5.1. Conclusions

First of all, a literature review on current state of surface roughness modeling was performed, with a special focus on turbomachinery application. Surface roughness modeling data is scattered with a wide variety of authors following different methodology depending on their specific applications. A summary with the main physical parameters used by different authors was made. These were defined and sketched in order to have a clear view of their different features. These set is given by: Ra, Rz, Rq, s_k, k_u, ES, λ, Λ_s, and α_{rms}. Moreover, the definition of the equivalent sandgrain roughness height, k_s, was given, defining the characteristic roughness ranges and the law of the wall. Literature on general surface roughness applications together with some others regarding turbomachinery applications was studied. Numerical and experimental studies were investigated to arrive to the selection of a physical-to-equivalent sandgrain correlation. The criteria followed to choose this correlation was based on the measurement complexity of the physical roughness variables, and the ability of these variables to model as many features of the roughness profile. Equation 2.14 was chosen as the best correlation to be used in further experimental and numerical studies in the frame of this project. The three variables used in this correlation (Rz, s_k and ES) are well known to cover a wide range of roughness features and do not present a high degree of complexity in terms of measurement procedures.

A mesh independence study was performed, developing a mesh capable of supporting the complete set of roughness cases. A validation of the results was performed comparing with available literature in the topic. The main effects of increasing surface roughness in a compressor stage were confirmed to be the increase in incidence angle, the change in passage shock location towards the LE, the reduction in strength of the passage shock, and the increase in width of the rotor and stator wakes. A reduction in stage pressure ratio, efficiency and mass flow ratio was confirmed for the same operating point, as well as an increase in overall blade loading.

Regarding the unsteady state simulations, the definition of flutter analysis setup was pre-

pared. Moreover, a validation of an initial or baseline case was computed to ensure that the main aerodynamic damping curve trends were maintained with respect to the reference case with no tip clearance.

Finally, the effects of surface roughness in the aerodynamic damping and wall work density were evaluated. Regarding the aerodynamic damping curve results, it has been shown that roughness does not change the overall shape of the curve, maintaining the minimum and maximum values at the same NDs. It has been demonstrated that roughness shifts the curve up or down depending on the ND. Most stable modes present a negative shift due to the increase in roughness. The opposite happens for the least stable modes, where roughness slightly improves the aeroelastic stability of the system. The WWD does not provide a clear idea of the phenomena leading to the changes in stability. Local changes are found mainly on the SS at locations close to the LE and the passage shock formation. Partial differences are better captured by analysing the unsteady pressure distribution, looking at its amplitude and phase distributions. Movement of the shock location, its strength and the change in incidence are the main contributions to the different computed aerodynamic damping values. The IBPA for the different ND also influences the final behavior of the system, as it shifts the distribution of the local phenomena happening on the stage.

5.2. Limitations

Limitations regarding the implementation of surface roughness just by the input of k_s can be identified. Primarily, the assumption of an evenly distributed surface roughness on the blade presents a poor representation of compressor rotor surface roughness in real applications, where blades show different roughness structures and heights depending on the location on the surface of the blade. A real used blade displays a higher roughness degree on the SS, close to the LE, while it features more scattered asperities on the PS. Furthermore, in recent studies it has been shown a higher influence of the asperities of the SS in the final performance of the machine. Another big limitation of this method is the roughness simulation as it is done by a simple shift of the wall. This simulates an extra blockage due to roughness. Although it is enough to model simple rough surfaces, it presents a lack of accuracy in terms of a poor modeling of roughness shape. This is why this drawback needs to be overcome by the selection of an accurate correlation with physical parameters.

Regarding the aerodynamic damping results, the poor representation of surface roughness just by an evenly distributed k_s may not be enough to provide an accurate study of roughness effects on the aeroelastic stability. Main drawback may arise from the tuned system assumption. This model presents a symmetric blade row, each blade featuring the same surface roughness

degree. This is far from reality. Surface roughness in a real machine rotor might be different from blade to blade, adding a certain degree of mistuning to the system, and can completely change the stability of the system due to the non-symmetric conditions.

5.3. Future Work

In addition to the previous limitations, some topics have not been covered or studied in detail in this thesis. In this section, they are going to be summarized in order to have a clear view of the main lines of work ahead:

- Contribution to a detailed investigation of surface roughness: The problem addressed in this thesis belongs to an initial stage for experimental and numerical studies with flat plates and real blades with implementation of surface roughness. Validation of surface roughness correlation with further measurements in real surfaces is required. Furthermore, it may be necessary to confirm the accuracy of the presented results through comparison with available experimental data in order to attain a certain level of confidence.

- Implementation of a non-constant roughness distribution on the blade: Using available data in blade surface roughness, it will be of a great interest to develop a model with a typical distribution on real blades. Moreover, implementing different roughness values for neighboring blades allowing to investigate the effect of a mistuned rotor due to roughness. Exploring the limits of surface roughness implementation in CFX, trying to exploit its capabilities to the maximum, and thus being able to save time by avoiding the use of DNS or expensive experimental procedures.

- Complete the aerodynamic damping curve and investigate other oscillation frequencies: Perform the completion of the aerodynamic damping S-curve, evaluating every nodal diameter to have a full understanding of the different variations in the effects of surface roughness. Also, recomputing the results for a different mode or performing a slight change in frequency might be also of interest. In this way, it may be also possible to see the trends in unstable nodal diameters, hence evaluating directly the impact on flutter inception.

- Further investigation of the compressor map shift due to surface roughness: An upper limit value was encountered when performing the steady-state simulations. As this project main objective was the identification of roughness effects on the aeroelastic stability, the investigation of this limit has been left for further studies on this topic.

BIBLIOGRAPHY

[1] R. Biollo and E. Benini, "Recent advances in transonic axial compressor aerodynamics," *Progress in Aerospace Sciences*, vol. 56, pp. 1–18, 2013. DOI: https://doi.org/10.1016/j.paerosci.2012.05.002. [Online]. Available: https://www.sciencedirect.com/science/article/pii/S0376042112000528.

[2] K. L. Suder *et al.*, "The Effect of Adding Roughness and Thickness to a Transonic Axial Compressor Rotor," *Journal of Turbomachinery*, vol. 117, no. 4, pp. 491–505, Oct. 1995. DOI: 10.1115/1.2836561. eprint: https://asmedigitalcollection.asme.org/turbomachinery/article-pdf/117/4/491/5840349/491_1.pdf. [Online]. Available: https://doi.org/10.1115/1.2836561.

[3] J. P. Bons, "A Review of Surface Roughness Effects in Gas Turbines," *Journal of Turbomachinery*, vol. 132, no. 2, Jan. 2010, 021004. DOI: 10.1115/1.3066315. eprint: https://asmedigitalcollection.asme.org/turbomachinery/article-pdf/132/2/021004/5754570/021004_1.pdf. [Online]. Available: https://doi.org/10.1115/1.3066315.

[4] S. Trevisani, G. Teza, and P. Guth, "A simplified geostatistical approach for characterizing key aspects of short-range roughness," *CATENA*, vol. 223, p. 106 927, 2023. DOI: https://doi.org/10.1016/j.catena.2023.106927. [Online]. Available: https://www.sciencedirect.com/science/article/pii/S0341816223000188.

[5] K. Bammert and G. U. Woelk, "The Influence of the Blading Surface Roughness on the Aerodynamic Behavior and Characteristic of an Axial Compressor," *Journal of Engineering for Power*, vol. 102, no. 2, pp. 283–287, Apr. 1980. DOI: 10.1115/1.3230249. eprint: https://asmedigitalcollection.asme.org/gasturbinespower/article-pdf/102/2/283/5638779/283_1.pdf. [Online]. Available: https://doi.org/10.1115/1.3230249.

[6] C. C. Koch and J. Smith L. H., "Loss Sources and Magnitudes in Axial-Flow Compressors," *Journal of Engineering for Power*, vol. 98, no. 3, pp. 411–424, Jul. 1976. DOI: 10.1115/1.3446202. eprint: https://asmedigitalcollection.asme.org/gasturbinespower/article-pdf/98/3/411/5643187/411_1.pdf. [Online]. Available: https://doi.org/10.1115/1.3446202.

[7] P. Gilge *et al.*, "Surface roughness of real operationally used compressor blade and blisk," *Proceedings of the Institution of Mechanical Engineers, Part G: Journal of Aerospace Engineering*, vol. 233, no. 14, pp. 5321–5330, 2019. DOI: 10.1177/0954410019843438. eprint: https://doi.org/10.1177/0954410019843438. [Online]. Available: https://doi.org/10.1177/0954410019843438.

[8] S.-H. Kang, Y.-S. Kang, and K.-H. Han, "Numerical study on blade roughness effect on the performance of turbomachines," in *Proceedings International Gas Turbine Congress, Tokyo, Japan*, 2003, pp. 2–7.

[9] E. Croner, O. Léon, and F. Chedevergne, "Industrial use of equivalent sand grain height models for roughness modelling in turbomachinery," in *55th 3AF International Conference on Applied Conference*, Poitiers, France, Apr. 2021. [Online]. Available: https://hal.science/hal-03228846.

[10] K. A. Flack and M. P. Schultz, "Review of Hydraulic Roughness Scales in the Fully Rough Regime," *Journal of Fluids Engineering*, vol. 132, no. 4, Apr. 2010, 041203. DOI: 10.1115/1.4001492. eprint: https://asmedigitalcollection.asme.org/fluidsengineering/article-pdf/132/4/041203/5516817/041203_1.pdf. [Online]. Available: https://doi.org/10.1115/1.4001492.

[11] R. Lechner and F. Menter, "Development of a rough wall boundary condition for ω-based turbulence models," Technical Report ANSYS/TR-04-04, Tech. Rep., 2004.

[12] A. Lipej, S. Muhič, and D. Mitruševski, "Wall roughness influence on the efficiency characteristics of centrifugal pump," *Strojniški vestnik - Journal of Mechanical Engineering*, vol. 63, no. 9, pp. 529–536, 2017. DOI: 10.5545/sv-jme.2017.4526. [Online]. Available: https://www.sv-jme.eu/article/wall-roughness-influence-on-the-efficiency-characteristics-of-centrifugal-pump/.

[13] J. Nikuradse *et al.*, "Laws of flow in rough pipes," 1950.

[14] H. Schlichting and J. Kestin, *Boundary layer theory*. Springer, 1961, vol. 121.

[15] M. Kadivar, D. Tormey, and G. McGranaghan, "A review on turbulent flow over rough surfaces: Fundamentals and theories," *International Journal of Thermofluids*, vol. 10, p. 100 077, 2021.

[16] M. N. Goodhand *et al.*, "The limitations of using "Ra" to describe surface roughness," *Journal of Turbomachinery*, vol. 138, no. 10, p. 101 003, 2016.

[17] J. P. Bons, "St and cf Augmentation for Real Turbine Roughness With Elevated Freestream Turbulence," *Journal of Turbomachinery*, vol. 124, no. 4, pp. 632–644, Nov. 2002. DOI: 10.1115/1.1505851. eprint: https://asmedigitalcollection.asme.org/turbomachinery/article-pdf/124/4/632/5529104/632_1.pdf. [Online]. Available: https://doi.org/10.1115/1.1505851.

[18] A. Schäffler, "Experimental and analytical investigation of the effects of reynolds number and blade surface roughness on multistage axial flow compressors," 1980.

[19] D. G. Bogard, D. L. Schmidt, and M. Tabbita, "Characterization and laboratory simulation of turbine airfoil surface roughness and associated heat transfer," in *Turbo Expo: Power for Land, Sea, and Air*, American Society of Mechanical Engineers, vol. 78750, 1996, V004T09A044.

[20] K. A. Flack *et al.*, "Skin-friction behavior in the transitionally-rough regime," *International Journal of Heat and Fluid Flow*, vol. 61, pp. 21–30, 2016.

[21] K. A. Flack, M. P. Schultz, and R. J. Volino, "The effect of a systematic change in surface roughness skewness on turbulence and drag," *International Journal of Heat and Fluid Flow*, vol. 85, p. 108 669, 2020.

[22] J. Bons, "A critical assessment of reynolds analogy for turbine flows," eng, *Journal of heat transfer*, vol. 127, no. 5, pp. 472–485, 2005.

[23] A. Sigal and J. E. Danberg, "New correlation of roughness density effect on the turbulent boundary layer," eng, *AIAA journal*, vol. 28, no. 3, pp. 554–556, 1990.

[24] E. Mainsah, J. Greenwood, and D. Chetwynd, *Metrology and Properties of Engineering Surfaces*. Jan. 2001. DOI: 10.1007/978-1-4757-3369-3.

[25] E. Napoli, V. Armenio, and M. de Marchis, "The effect of the slope of irregularly distributed roughness elements on turbulent wall-bounded flows," *Journal of Fluid Mechanics*, vol. 613, pp. 385–394, 2008. DOI: 10.1017/S0022112008003571.

[26] M. MacDonald *et al.*, "Turbulent flow over transitionally rough surfaces with varying roughness densities," *Journal of Fluid Mechanics*, vol. 804, pp. 130–161, 2016. DOI: 10.1017/jfm.2016.459.

[27] M. I. Khan, "The influence of two-dimensional bed roughness on the flow structure of a turbulent boundary layer," 2004.

[28] M. Thakkar, A. Busse, and N. Sandham, "Surface correlations of hydrodynamic drag for transitionally rough engineering surfaces," *Journal of Turbulence*, vol. 18, no. 2, pp. 138–169, 2017. DOI: 10.1080/14685248.2016.1258119. [Online]. Available: https://doi.org/10.1080/14685248.2016.1258119.

[29] ISO, *4287: 1997: Geometrical product specifications (GPS)–Surface texture: profile method–Terms, definitions and surface texture parameters*. 1998.

[30] K. Flack, M. Schultz, and J. Barros, "Skin friction measurements of systematically-varied roughness: Probing the role of roughness amplitude and skewness," *Flow, Turbulence and Combustion*, vol. 104, pp. 317–329, 2020.

[31] M. Acharya, J. Bornstein, and M. Escudier, "Turbulent boundary layers on rough surfaces," *Experiments in Fluids*, vol. 4, pp. 33–47, 1986.

[32] J. A. van Rij, B. J. Belnap, and P. M. Ligrani, "Analysis and Experiments on Three-Dimensional, Irregular Surface Roughness," *Journal of Fluids Engineering*, vol. 124, no. 3, pp. 671–677, Aug. 2002. DOI: 10.1115/1.1486222. [Online]. Available: https://doi.org/10.1115/1.1486222.

[33] M. Schultz and K. Flack, "Outer layer similarity in fully rough turbulent boundary layers," *Experiments in fluids*, vol. 38, pp. 328–340, 2005.

[34] K. A. Flack and M. P. Schultz, "Roughness effects on wall-bounded turbulent flows," *Physics of Fluids*, vol. 26, no. 10, p. 101 305, 2014.

[35] P. Forooghi *et al.*, "Toward a universal roughness correlation," *Journal of Fluids Engineering*, vol. 139, no. 12, 2017.

[36] J. Belz and H. Hennings, "Experimental flutter investigations of an annular compressor cascade: Influence of reduced frequency on stability," in *Unsteady Aerodynamics, Aeroacoustics and Aeroelasticity of Turbomachines*, K. C. Hall, R. E. Kielb, and J. P. Thomas, Eds., LIDO-Berichtsjahr=2004, Springer, 2006, pp. 77–91. [Online]. Available: https://elib.dlr.de/14417/.

[37] D. Vogt, "Experimental investigation of three-dimensional mechanisms in low-pressure turbine flutter," Ph.D. dissertation, KTH, Energy Technology, 2005, p. 189.

[38] F. Holzinger *et al.*, "Self-Excited Blade Vibration Experimentally Investigated in Transonic Compressors: Rotating Instabilities and Flutter," *Journal of Turbomachinery*, vol. 138, no. 4, Jan. 2016, 041006. DOI: 10.1115/1.4032163. eprint: https://asmedigitalcollection.asme.org/turbomachinery/article-pdf/138/4/041006/6303460/turbo_138_04_041006.pdf. [Online]. Available: https://doi.org/10.1115/1.4032163.

[39] A. V. Srinivasan, "Flutter and Resonant Vibration Characteristics of Engine Blades," *Journal of Engineering for Gas Turbines and Power*, vol. 119, no. 4, pp. 742–775, Oct. 1997. DOI: 10.1115/1.2817053. eprint: https://asmedigitalcollection.asme.org/gasturbinespower/article-pdf/119/4/742/5889496/742_1.pdf. [Online]. Available: https://doi.org/10.1115/1.2817053.

[40] Y. El-Aini *et al.*, "High cycle fatigue of turbomachinery components - industry perspective," in *33rd Joint Propulsion Conference and Exhibit*. DOI: 10.2514/6.1997-3365. eprint: https://arc.aiaa.org/doi/pdf/10.2514/6.1997-3365. [Online]. Available: https://arc.aiaa.org/doi/abs/10.2514/6.1997-3365.

[41] M. Saber and M. Djavareshkian, "Investigating the effect of roughness and stiffness in 2d aeroelastic around oscillatory airfoil," *WSEAS TRANSACTIONS ON APPLIED AND THEORETICAL MECHANICS*, vol. 15, pp. 140–150, Oct. 2020. DOI: 10.37394/232011.2020.15.16.

[42] E. Politis *et al.*, *KNOW-BLADE task-4 report: Navier-Stokes aeroelasticity* (Denmark. Forskningscenter Risoe. Risoe-R 1492(EN)), English. 2004.

[43] A. R. Collar, "The expanding domain of aeroelasticity," *The Aeronautical Journal*, vol. 50, no. 428, pp. 613–636, 1946. DOI: 10.1017/S0368393100120358.

[44] M. Gutierrez Salas, "Development of accurate reduced order models in a simulation tool for turbomachinery aeromechanical phenomena," QC 20180514, Ph.D. dissertation, KTH, Heat and Power Technology, 2018, p. 68.

[45] G. Yi *et al.*, "Geometry-load based hybrid correction method for the pre-deformation design of a steam turbine blade," *Energies*, vol. 13, no. 10, 2020. DOI: 10.3390/en13102471. [Online]. Available: https://www.mdpi.com/1996-1073/13/10/2471.

[46] F. Holzinger *et al.*, "Self-Excited Blade Vibration Experimentally Investigated in Transonic Compressors: Acoustic Resonance," *Journal of Turbomachinery*, vol. 138, no. 4, p. 041 001, Dec. 2015. DOI: 10.1115/1.4032042. eprint: https://asmedigitalcollection.asme.org/turbomachinery/article-pdf/138/4/041001/6303626/turbo_138_04_041001.pdf. [Online]. Available: https://doi.org/10.1115/1.4032042.

[47] M. Baumgartner, F. Kameier, and J. Hourmouziadis, "Non-Engine Order Blade Vibration in a High Pressure Compressor," in *Twelfth International Symposium on Airbreathing Engines*, Melbourne, Australia, Sep. 1995. [Online]. Available: https://hal.science/hal-01353829.

[48] C. Brandstetter, M. Jüngst, and H.-P. Schiffer, "Measurements of Radial Vortices, Spill Forward and Vortex Breakdown in a Transonic Compressor," ser. Turbo Expo: Power for Land, Sea, and Air, vol. Volume 7B: Structures and Dynamics, Jun. 2017, V07BT36A018. DOI: 10.1115/GT2017-64576. eprint: https://asmedigitalcollection.asme.org/GT/proceedings-pdf/GT2017/50930/V07BT36A018/4239765/v07bt36a018-gt2017-64576.pdf. [Online]. Available: https://doi.org/10.1115/GT2017-64576.

[49] J. F. Lubomski, "Status of nasa full-scale engine aeroelasticity research," in *Structures, Structural Dynamics and Materials Conference (Seattle)*, 1980.

[50] A. Vega Coso, "Impact of the unsteady aerodynamics of oscillating airfoils on the flutter characteristics of turbomachines," 2016. DOI: 10.20868/UPM.thesis.44502. [Online]. Available: https://oa.upm.es/44502/.

[51] P. Duquesne *et al.*, "Choke flutter instability sources tracking with linearized calculations," *International Journal of Numerical Methods for Heat & amp Fluid Flow*, vol. 30, no. 9, pp. 4155–4166, Jan. 2019. DOI: 10.1108/hff-06-2018-0281. [Online]. Available: https://doi.org/10.1108%5C%2Fhff-06-2018-0281.

[52] E. H. Dowell *et al.*, "Stall flutter," in *A modern course in aeroelasticity*, E. H. Dowell *et al.*, Eds. Dordrecht: Springer Netherlands, 1989, pp. 270–289. DOI: 10.1007/978-94-015-7858-5_5. [Online]. Available: https://doi.org/10.1007/978-94-015-7858-5_5.

[53] E. H. Dowell, "Aeroelasticity in turbomachines," in *A Modern Course in Aeroelasticity: Fifth Revised and Enlarged Edition*. Cham: Springer International Publishing, 2015, pp. 409–438. DOI: 10.1007/978-3-319-09453-3_8. [Online]. Available: https://doi.org/10.1007/978-3-319-09453-3_8.

[54] H. Ferria, "Contribution to numerical and experimental studies of flutter in space turbines : aerodynamic analysis of subsonic and supersonic flows in response to a prescribed vibratory mode of the structure," Theses, Ecole Centrale de Lyon ; Kungliga tekniska högskolan (Stockholm), Feb. 2011. [Online]. Available: https://theses.hal.science/tel-00677648.

[55] C. Tavera Guerrero, "Final work : Flutter wizard: Development of an automatic tool for safety prediction in compressors and turbines," 2019.

[56] C. Prasad and L. Pešek, "Analysis of classical flutter in steam turbine blades using reduced order aeroelastic model," *MATEC Web of Conferences*, vol. 211, p. 15 001, Jan. 2018. DOI: 10.1051/matecconf/201821115001.

[57] G. Politakis, W. Haans, and G. van Bussel, "Suppression of classical flutter using a 'smart blade'," *46th AIAA Aerospace sciences meeting and exhibit, Reno, Jan.*, Jan. 2008. DOI: 10.2514/6.2008-1301.

[58] S. Patil *et al.*, "Investigation of Time/Frequency Domain CFD Methods to Predict Turbomachinery Blade Aerodynamic Damping," ser. Turbo Expo: Power for Land, Sea, and Air, vol. Volume 7B: Structures and Dynamics, Jun. 2016, V07BT34A028. DOI: 10.1115/GT2016-57962. eprint: https://asmedigitalcollection.asme.org/GT/proceedings-pdf/GT2016/49842/V07BT34A028/4239681/v07bt34a028-gt2016-57962.pdf. [Online]. Available: https://doi.org/10.1115/GT2016-57962.

[59] F. O. Carta, "Coupled Blade-Disk-Shroud Flutter Instabilities in Turbojet Engine Rotors," *Journal of Engineering for Power*, vol. 89, no. 3, pp. 419–426, Jul. 1967. DOI: 10.1115/1.3616708. eprint: https://asmedigitalcollection.asme.org/gasturbinespower/article-pdf/89/3/419/5804992/419_1.pdf. [Online]. Available: https://doi.org/10.1115/1.3616708.

[60] M. Lejon *et al.*, "Multidisciplinary Design of a Three Stage High Speed Booster," ser. Turbo Expo: Power for Land, Sea, and Air, vol. Volume 2B: Turbomachinery, Jun. 2017, V02BT41A037. DOI: 10.1115/GT2017-64466. eprint: https://asmedigitalcollection.asme.org/GT/proceedings-pdf/GT2017/50794/V02BT41A037/2432296/v02bt41a037-gt2017-64466.pdf. [Online]. Available: https://doi.org/10.1115/GT2017-64466.

[61] T. Grönstedt, N. Andersson, and M. Lejon, *Vink 1.0.0*, version v1.0.0, Zenodo, Sep. 2017. DOI: 10.5281/zenodo.896277. [Online]. Available: https://doi.org/10.5281/zenodo.896277.

[62] N. R. Vadlamani, P. G. Tucker, and P. Durbin, "Distributed roughness effects on transitional and turbulent boundary layers," *Flow, Turbulence and Combustion*, vol. 100, no. 3, 627ndash, 649, Oct. 2017. DOI: 10.1007/s10494-017-9864-4. [Online]. Available: https://doi.org/10.1007%2Fs10494-017-9864-4.

[63] ANSYS Inc., "Cfx-solver theory guide," *Release 2021 R2*, 2023.

[64] F. Menter, "Zonal two equation k-w turbulence models for aerodynamic flows," in *23rd Fluid Dynamics, Plasmadynamics, and Lasers Conference*. DOI: 10.2514/6.1993-2906. eprint: https://arc.aiaa.org/doi/pdf/10.2514/6.1993-2906. [Online]. Available: https://arc.aiaa.org/doi/abs/10.2514/6.1993-2906.

[65] F. R. Menter, "Two-equation eddy-viscosity turbulence models for engineering applications," *AIAA Journal*, vol. 32, no. 8, pp. 1598–1605, 1994. DOI: 10.2514/3.12149. eprint: https://doi.org/10.2514/3.12149. [Online]. Available: https://doi.org/10.2514/3.12149.

[66] ANSYS Inc., "Cfx-solver modeling guide," *Release 2021 R2*, 2023.

[67] ANSYS Inc., "Cfx tutorials," *Release 2021 R2*, 2023.

[68] *On Improving the Surge Margin of a Tip-Critical Axial Compressor Rotor*, vol. Volume 2A: Turbomachinery, Turbo Expo: Power for Land, Sea, and Air, Jun. 2017, V02AT39A035. DOI: 10.1115/GT2017-64533. eprint: https://asmedigitalcollection.asme.org/GT/proceedings-pdf/GT2017/50787/V02AT39A035/2432164/v02at39a035-gt2017-64533.pdf. [Online]. Available: https://doi.org/10.1115/GT2017-64533.

[69] D. Vogt, "Turbomachinery aeromechanics: An introduction and a few examples of interest," *Aeromechanic Project Course slides. KTH - Royal Institute of Technology, Stockholm*, Jan. 2021.